Mechanical Resonators Based on Graphene and Carbon Nanotubes

Thesis by
Ioannis Tsioutsios

June 2016

Doctoral school in Physics, Universitat Autònoma de Barcelona (UAB)
ICFO - The Institute of Photonic Sciences

Supervisor: Prof. Dr. Adrian Bachtold
Tutor: Prof. Dr. Jordi Pascual Gainza

Thesis committee:
Prof. Dr. Francisco Javier Tamayo de Miguel
Prof. Dr. Jean-Philippe Poizat
Prof. Dr. Romain Quidant

ICFO
Institut
de Ciències
Fotòniques

UAB
Universitat Autònoma
de Barcelona

Chapter 5

Coupled Graphene Mechanical Resonators

This chapter is based on the work that has been published in Ref. [95], where we study coupled graphene mechanical resonators.

In the first section we give a brief introduction on coupled mechanical resonators and the motivation towards studying coupled mechanical systems based on graphene and carbon nanotubes. We will then describe the fabrication process steps of such systems. Afterwards, we will present the main experimental results starting from characterizing the electrical and mechanical properties of the studied devices. We will then identify and fully characterize their eigenmodes and discuss the observation of nonlinear coupling between them explaining this effect by introducing a basic theoretical modelling which is presented in detail in Appendix A. Finally, we present the results of finity element simulation of the devices and we compare them with the experimental and the theoretical modelling predictions.

5.1   Introduction

The interest on studying the motion of coupled mechanical oscillators is very old and has both fundamental and technological aspects. The first studies can be traced back as early as in the mid-seventeenth century, where Christiaan Huygens studied novel dynamics in a pair of coupled pendulum clocks [96]. By hanging them on a common support, he observed that they exhibit synchronized oscillations and this allows to increase their precision and stability.

In the area of nanotechnology and nanoscience, research on coupled micro- and nanomechanical resonators has attracted considerable attention. Coupling their mechanical motion can give rise to rich linear and nonlinear dynamics such as vibration localization [97], synchronization [98], nonlinear mode coupling and chaos [60], paramateric mode splitting and coherent phonon manipulation [99]. In the quantum regime [7, 8, 100, 101], nonlinear mode coupling has been proposed as a way to perform quantum non-demolition measurements [102]. From the technological point of view, coupled nanomechanical resonators have been a subject of intense interest due to their high potential as high-quality factor resonators [103] and band pass filters [104], mass and charge sensors with high sensitivity
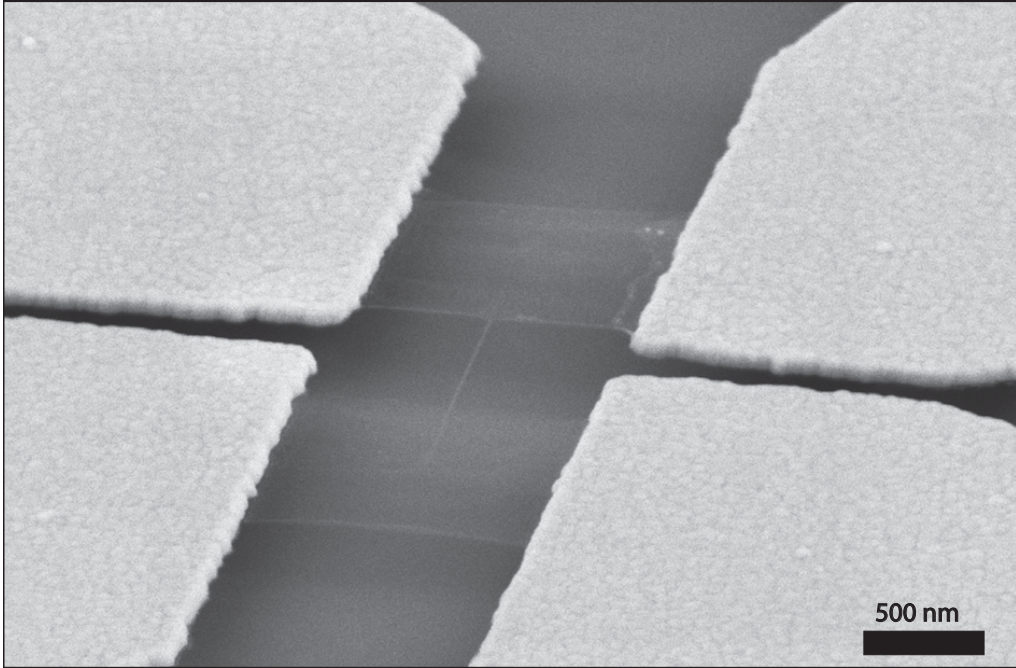
Figure 5.1: Scanning electron microscopy image of a coupled graphene resonator device. Two grpahene membranes are susbended and each of them is doubly-clamped by two gold electrodes. A multiwall carbon nanotube is linking the two graphene membranes at their middle in an H-shape configuration.

[105, 106, 107, 5], signal amplifiers [108], and logic gates [72].

So far, most of the research attention on coupled nanoresonators, has been mainly concentrated on system that are implemented using top-down nanofabrication techniques. On the other hand, bottom-up fabricated nanoresonators based on nanomaterials like graphene and carbon nanotubes possess a wide variety of outstanding properties [109, 18, 24, 25, 22, 19, 13, 110]. These systems can be employed as sensitive mass detectors [20], their resonance frequency can exceed 10 GHz [14, 15], they exhibit strong mechanical nonlinearities [13, 29, 30], and their mechanical vibrations can efficiently couple to electrons in the Coulomb blockade and the quantum Hall regimes [24, 25, 26, 27, 28].

However, the wealth of graphene and carbon nanotube properties have not yet been extensively studied in systems where two or more of those devices are coupled. A first step in this direction was made by Perisanu *et al.* (2011) [111] where they investigated the coupling between two vibrating nanotubes by gluing several nanotubes on a tip and imaging them in a transmission electron microscope [111]. Nonetheless, it is important to develop coupled vibrational structures with a well-defined layout in order to enable experiments where nonlinear dynamics, manipulation of mechanical states, and quantum non-demolition measurements, are performed in a controlled way. The challenge presented by the fabrication of such structures is that nanotubes and graphene cannot be structured as easily as other materials. Indeed, graphene can be patterned into complicated shapes using electron-beam lithography and reactive ion etching, but such graphene structures

are fragile and often tear when suspended. As for nanotubes, it is very difficult to place them at a predetermined position.

In this chapter, we demonstrate the fabrication and we study the dynamics of coupled graphene mechanical resonators. These devices consist of two doubly-clamped graphene mechanical resonators which are linked by a nanotube beam, while the whole structure is suspended (Figure 5.1). The structure is fabricated using a combination of electron-beam lithography and atomic-force microscopy nano-manipulation. Each graphene plate is clamped by two metal electrodes so that mechanical vibrations can be independently actuated and detected electrically using mixing techniques [18, 77]. Two mechanical eigenmodes are measured, each corresponding to vibrations localized in a different graphene resonator. The coupling between the eigenmodes is evaluated by measuring the shift of the resonance frequency of the one eigenmode as a function of the estimated vibration amplitude of the other eigenmode.

5.2 Fabrication

In Figure 5.2 the fabrication process flow of coupled graphene mechanical resonators devices is illustrated. Each process step is separately explained in a more detailed way below.
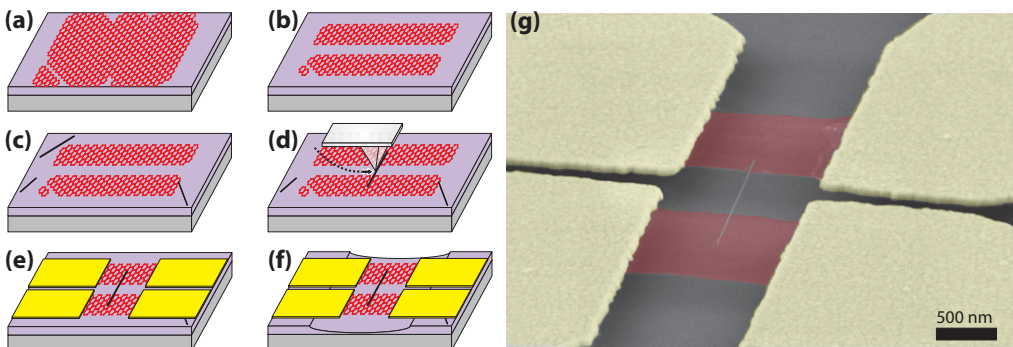

Figure 5.2: Fabrication of two graphene resonators coupled by a carbon nanotube. **(a)** Mechanical exfoliation of graphene onto an oxidized silicon wafer. **(b)** Shaping the graphene layer with reactive ion etching. **(c)** Deposition of nanotubes. **(d)** Manipulation of a nanotube with an AFM tip. **(e)** Patterning of metal electrodes using electron-beam lithography. **(f)** Removal of the silicon oxide below the structure with hydrofluoric acid. **(g)** Colorized scanning electron microscope image of the device at the end of the fabrication process.

(a) Graphene exfoliation

The fabrication process starts by depositing graphene flakes on highly doped, oxidized silicon wafers using the mechanical exfoliation technique (Figure 5.2(a)) [31] [1]. Single and bilayer graphene flakes are selected with an optical microscope by measuring the intensity of the reflected light, as illustrated in Figure 5.3. The contrast depends on the amount

---

[1]Before the exfoliation step, it is very important that the silicon oxide substrate surface is as clean as possible. For these reason the chips are sonicated in an aceton bath and then in an isopropyl alcohol bath. Afterworlds an oven annealing step follows, under Ar and H_2 flow at 300 ^{o}C.

of graphene layer and the thickness of the silicon oxide substrate. The intensity for each substrate is calibrated after characterizing single and few graphene layers with Raman spectroscopy. The silicon oxide thickness for this specific type of devices is selected to be 435 nm. This specific thickness provides less optical contrast compared to the commonly used 285 nm thickness [112]. However, it provides enough thickness in order to etch the silicon oxide under big graphene structures, while still leaving a part of it and avoid any short-circuits to the back gate from other graphene flakes or nanotubes that are on the chip (see the last fabrication step).
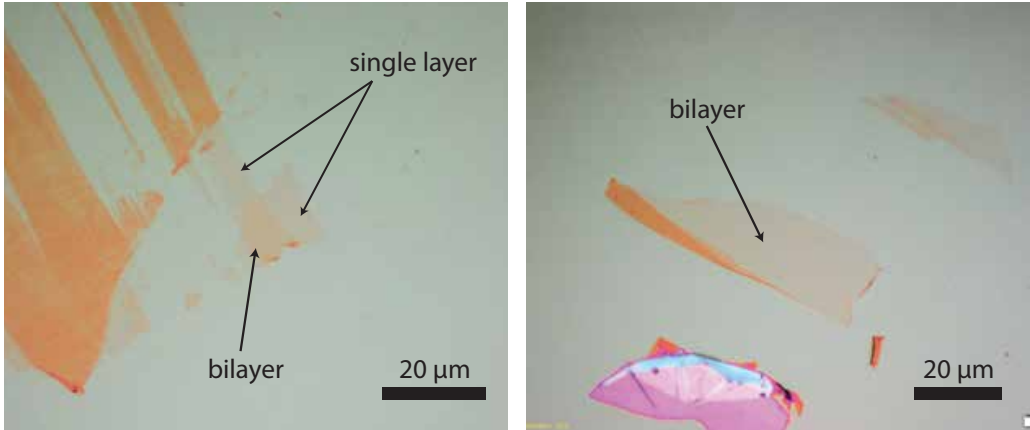

Figure 5.3: Optical images of graphene mechanically exfoliated on oxidized silicon substrate. The silicon oxide thickness is selected to be 435 nm. Left: Single and bilayer graphene. Righ: The bilayer graphene flake that was used for the device that is illustrated in Figure 5.1.

(b) Graphene patterning

Each flake is patterned into two parallel rectangular plates using electron-beam lithography (EBL) and reactive ion etching in oxygen (Figure 5.2(b)). In order to be able to localize graphene on the chip, we first pattern Au/Cr marks by Electron Beam Lithography (EBL), metal deposition, and lift-off (Figure 5.4(a)). The marks are then used for the alignment process during the electron-beam lithography step, where a PMMA 950 mask is used to shape graphene using reactive ion etching (Figure 5.4(b)).

(c) Carbon nanotubes deposition

A dichloroethane solution containing multi-walled carbon nanotubes is spin-cast onto the wafer (Figure 5.2(c)). As a result, several nanotubes are found near the already patterned graphene flakes (Figure 5.4(b)). We also noticed an increased adhesion rate of nanotubes in the area around graphene that has been exposed in RIE.

(d) Carbon nanotubes positioning with AFM

The tip of an atomic force microscope (AFM) probe is then used, in contact mode, to position a multi-walled carbon nanotube across the two graphene plates (Figure 5.2(d))
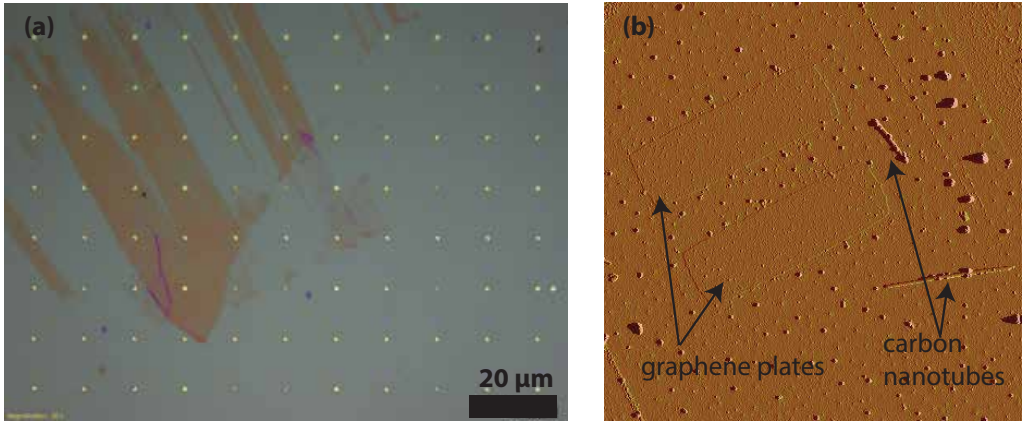
Figure 5.4: (a) Optical image of graphene flake with Au/Cr alignement marks. (b)Atomi force microscopy image of graphene shaped into to two graphene plates. Carbon nanotubes are found next to them, after spin-cast deposition.

[113, 114]. This allows to push the nanotube from the one side and place it at the desired position [2]. In Figure 5.5 the manipulation process is illustrated in a series of AFM images.
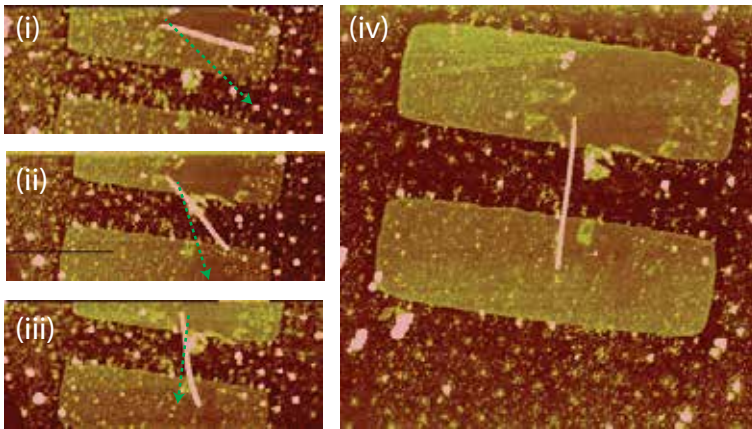

Figure 5.5: Carbon nanotube positioning. A series of AFM images (i-iv) that illustrate the consecutive steps that are needed to place the multiwall carbon nanotube across the two grpahene plates. The green arows indicates the path that the AFM tip follows, in contact mode, during each manipulation step.

(e) Electrodes deposition

Each graphene plate is contacted to a pair of Au/Cr electrodes by EBL, metal deposition, and lift-off (Figure 5.2(e), Figure 5.6(a)).

---

[2]A key point for the success of the nanomanipulation process is that the force that is applied from the AFM tip towards the substrate is well calibrated. It should be high enough to push the nanotube from the side, while low enough in order not to damage the graphene.

(f) Structure suspension

The graphene plates and the nanotube are suspended by etching 260 nm of the underlying silicon oxide in hydrofluoric acid. A PMMA 950 mask created with an e-beam lithography has been used in order to etch the oxide only locally at the area where the device stands (Figure 5.2(f), Figure 5.6(b)). The structure is released in a critical point drier in order to avoid its collapsing due to capillary forces. The highly doped silicon substrate is used as a backgate. Figure 5.2(g) shows a colorized scanning electron microscope image of a device made from a bilayer graphene sheet upon completion of the fabrication process.
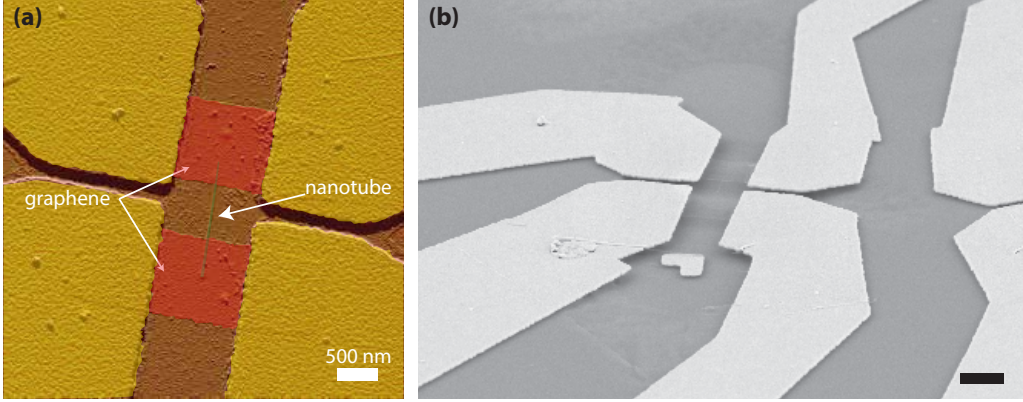

Figure 5.6: **(a)** Colorized atomic force microscopy image of a bilayer coupled graphene resonators device after electrods deposition. The Au/Cr electrode are colorized with yellow, graphen plates with red, and the carbon nanotube with green. **(b)** Scanning electron microscopy of the device after the critical point drying step. The whole graphene and nanotube structure is suspended on top of the substrate. The silicon oxide is only locally etched in the area of the structure.

5.3 Experimental results

5.3.1 Experimental setup

The experimental setup consist of a home-build flow cryostat (Figure 5.7(a)). The sample is attached to the cold finger of a liquid helium insert (Janis, ST-400). The measurements have been carried out at 4.2 K (Helium flow) at a pressure of $\sim 10^{-8}$ mbar. The sample is clamped on a printed circuit board which is electrically connected with three RF lines (SMA) and two 2 DC lines (Figure 5.7(b)). Since the devices have a global back-gate, which means that there are increased parasitic capacitances, we selected to perform our experiments using frequency mixing techniques (see subsection 4.2.4) and mainly the frequency modulation (FM) mixing technique [77]. The source electrode of each graphene plate is connected to a separate RF line. The third RF line is connected to the doped silicon substrate which act as a global back-gate. Each drain electrode is connected to a separate DC line, where the low frequency mixing current is measured for each graphene plate independently. For each DC line, an on-PCB low pass filter has been implemented in order to avoid noise from high order mixing components. This electrical configuration enables us to actuate and detect the vibration of each graphene plate independently.
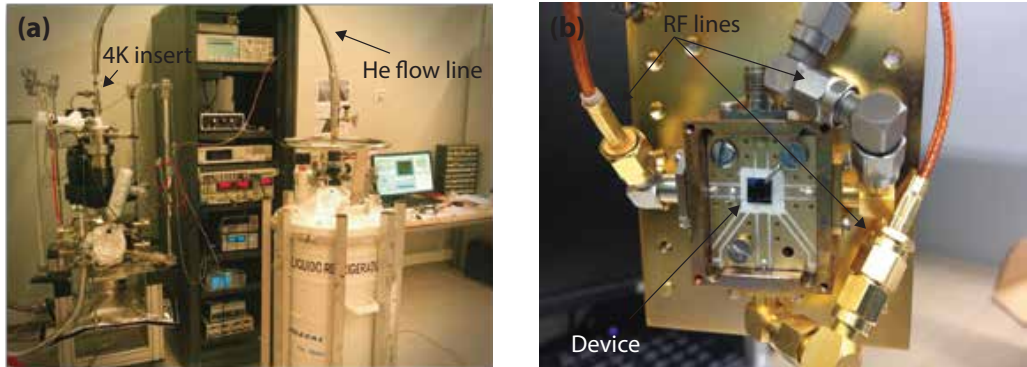
Figure 5.7: Experimental setup. **(a)** Optical image of the flow cryostat that was used for the experiment. **(b)** Optical image of the PCB used for the devices measurement. It is clamped at the lower part of the cryostat cold figure.

5.3.2 Electrical properties characterization

Three operating devices were fabricated. We first present measurements obtained with one of them at a temperature of 4.2 K. The two graphene plates have the same length of 1.14 μm (between the clamping electrodes) and the same width of 1 μm. The length of the nanotube is 1.74 μm and its diameter is 17 nm. The electrical two-point resistances of the two graphene plates range from 40 to 100 kΩ. In comparison, the resistance of the multi-walled carbon nanotube measured between the two graphene resonators is about 1MΩ, and is therefore much larger. Thus, the electrical current flowing through the nanotube is negligible in the measurements discussed below.

The transconductance characteristics of the devices were studied in order the select the best operating point that maximizes signal. Figure 5.8 shows the conductance of each graphene plate as a function of the voltage applied to the back-gate, for the first device. The modulation of the conductance is attributed to universal conductance fluctuations (UCF). This layout allows to electrically detect the mechanical vibrations of the two graphene plates using the frequency-modulation mixing technique (see section 4.2.4). According to the expression (4.26), the mixing current I_{mix} associated to the motion of each graphene plate, depends on the transconductance and on the back-gate biasing (V_{BG}). For each graphene plate there is a specific value of V_{BG} that maximizes the mixing current.

In order to minimize the consumption of liquid helium, the cryostat is warmed up overnight. The mechanical properties of the device change only slightly from one day to the next. For instance, the resonance frequency changes by less than 10%. However, the changes in the electrical properties are significant. In particular, the universal conductance fluctuations are completely different from one day to the next, and so is the value of V_{BG} for which the mixing current is largest.

5.3.3 Eigenmodes characterization

A system of two coupled nonlinear (duffing) mechanical resonators can be modeled by introducing a linear coupling term, $D(x_1 - x_2)$, into their individual equations of motion
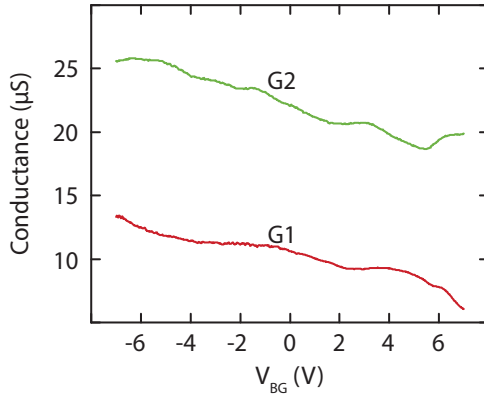
Figure 5.8: Conductance versus back-gate voltage for the two graphene plates at 4.3 K.

(eq. 3.25) [3]:

$$\ddot{x}_1 + \gamma_1 \dot{x}_1 + \omega_1^2 x_1 + \alpha_1 x_1^3 + D(x_1 - x_2) = F_1(t)/m$$
$$\ddot{x}_2 + \gamma_1 \dot{x}_2 + \omega_2^2 x_2 + \alpha_2 x_2^3 + D(x_2 - x_1) = F_2(t)/m, \tag{5.1}$$

where D is the coupling strength. This set of equations predicts two eigenmodes (for more information see Appendix A), an in-phase eigenmode I, where the two resonators are vibrating with the same phase, and an out of phase eigenmode II where the two resonators are vibrating at a higher frequency ($f_{II}^0 > f_I^0$) but with 180 degrees phase difference. If the two individual (uncoupled) resonators 1 and 2 are identical ($f_2^0 - f_1^0 = 0$), the amplitude of both I and II eigenmodes is delocalized between the two resonators. If $f_2^0 > f_1^0$, both the in-phase and out of phase eigenmodes still exist, but the amplitude of eigenmode I is more localized on the first resonator and the amplitude of eigenmode II on the second.

We first characterize the devices by identifying their eigenmodes and eigenfrequencies. To do so, one individual graphene resonator is actuated and its vibrations are detected using the frequency modulation (FM) mixing technique [77] (section 4.2.4), while the other graphene resonator is kept electrically floating. In this transduction scheme (Figure 5.9), the measured mixing current (I_{mix}), each time is only proportional to the motion of each individual resonator. This allows us to identify where, between the two graphene resonators, the amplitude of each eigenmode is localized.

Figure 5.9 shows one prominent mechanical resonance in the spectrum of each individually driven graphene resonator. This result is in agreement with the theory of two coupled mechanical resonators, and indicates that the amplitude A_I, of eigenmode I, is mainly localized on graphene 1, and the amplitude A_{II}, of eigenmode II, on graphene 2 [4]. Interestingly, the resonances appear at two distinct frequencies, $f_I^0 \approx 140$ MHz and $f_{II}^0 \approx 180$ MHz. This frequency difference and the localization of the eigenmodes, suggests that the elastic coupling between the two eigenmodes is weak ($f_2^{0^2} - f_1^{0^2} \gg D$),

---

[3] A detailed analysis on the dynamics of coupled mechanical resonators is given in Appendix A.

[4] In order to avoid any confusion, we use the notation I, II for the eigenmodes of the coupled system, while $1, 2$ for the individual resonators (see Figure 5.9).
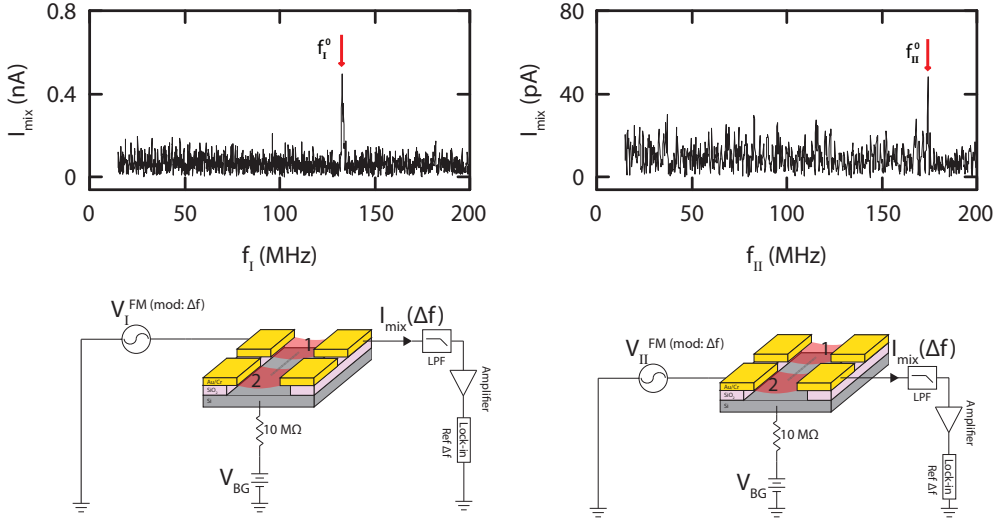
Figure 5.9: Characterizing the coupled resonator made from a single layer graphene sheet. Mechanical spectrum of graphene resonator 1 and 2 (obtained by measuring the mixing current I_{mix} as a function of the driving frequency). Eigenmode I is localised in graphene resonator 1 and eigenmode II in graphene resonator 2. The gate voltage V_{BG} is $5\,\mathrm{V}$ for the upper spectrum and $-4\,\mathrm{V}$ for the lower spectrum. The quality factors are $Q_I = 5500$ and $Q_{II} = 4000$ for plates 1 and 2, respectively. V_{II}^{FM} and V_{II}^{FM} are the amplitudes of the FM oscillating voltages.

see section A.1). In other words, the carbon nanotube transfers the vibrations of one graphene resonator to the other only weakly [105, 106], and the eigenmode frequencies $(f_{I,II}^0)$ are very close to the frequencies of individual graphene resonator $(f_{1,2}^0)$. Similar results are obtained with the two other measured devices. We note that in Figure 5.9, the two graphene resonators feature different current amplitudes on resonance as well as different background noises; this is attributed to the different electrical properties of the two graphene resonators (see subsection 5.3.2).

5.3.4 Mechanical properties characterization

The graphene membranes are found to be under tensile stress by measuring their resonance frequency f_0 as a function of the constant voltage V_{BG} applied to the backgate (Figure 5.10). The resonance frequency decreases quadratically upon increasing V_{BG}. Similar results were obtained in previous measurements on single graphene resonators at low temperature [19, 13, 115]. The convex parabola has an electrostatic origin and indicates that the graphene membrane is under tensile stress because of the metal electrodes, which contract upon lowering the temperature. The tension T_0 within each graphene membrane can be quantified by fitting the V_{BG} dependence of the resonance frequency to the expression derived for a resonator under tensile stress, $f_0(V_{\mathrm{BG}}) = f_{\max} - \sigma V_{\mathrm{BG}}^2$, where $f_{\max} = \frac{1}{2}\sqrt{T_0/mL}$ and $\sigma = f_{\max} C'' L/(4\pi^2 T_0)$. Here, m is the mass of the resonator, L its length, and C'' the second derivative of the graphene-gate capacitance with respect
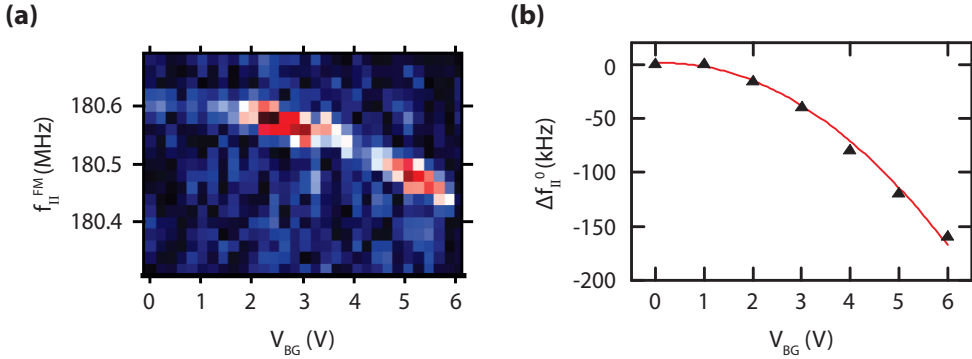
(a)

(b)

Figure 5.10: Back gate dependance of the second eigenmode (f_{II}^0). **(a)** Mixing current as a function of the carrier frequency and V_{BG}. The amplitude of the mixing current oscillates as a function of V_{BG} in an aperiodic way due to universal conductance fluctuations. **(b)** Resonance frequency shift of the second mode (f_{II}^0) as a function of V_{BG}.

to displacement. The term $-\sigma V_{BG}^2$ originates from the plate oscillating in an BG electric field gradient. We find that the tension is 713 nN and 883 nN and the mass is 7.8 fg and 5.8 fg for graphene membrane 1 and 2, respectively. The corresponding mass densities are 9.2 and 6.9 times larger than that of pristine graphene, suggesting contamination of the graphene surface. Similar values of tensions and mass densities were found in previous measurements on single graphene resonators [19, 13, 115]. This further supports our finding that the nanotube affects the resonance of the individual graphene resonators only weakly. The difference in mass density between the two graphene membranes may be attributed to the partial cleaning of the contamination during the manipulation of the nanotube with the AFM tip during the fabrication of the device [116].

5.3.5 Duffing nonlinearity

The response of each eigenmode for high driving amplitude shows nonlinear behavior. Figure 5.11(a) displays the mixing current for eigenmode I as a function of increasing driving frequency and for various amplitudes of the driving force. The driving force is proportional to V_I^{FM} [[77]], the amplitude of the frequency-modulated voltage used to drive the first graphene resonator. As V_I^{FM} is increased, the resonance lineshape becomes asymmetric and its peak frequency increases. The resonance frequency is determined as the frequency for which the current measured with the FM mixing technique is largest (we verified that this frequency is nearly equal to the frequency for which the motional amplitude is largest by solving the equation of motion numerically [13]). The dependence of the peak frequency on V_I^{FM} is shown in Figure 5.11(b). This behavior is attributed to the Duffing force that originates from the mechanical tension within the graphene membrane at large motional amplitude; because it is clamped at both ends, graphene stretches and compresses periodically in time.
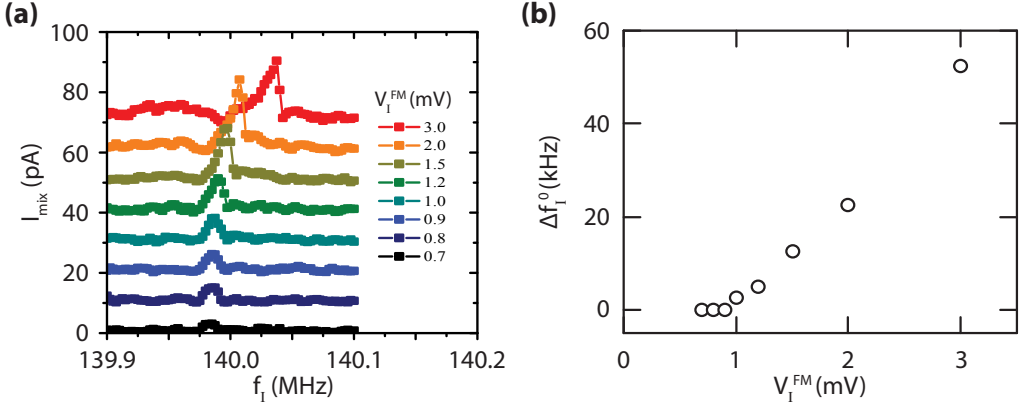
Figure 5.11: Nonlinear (Duffing) resonance. **(a)** Mixing current for eigenmode I as a function of increasing driving frequency f and for various amplitudes of the driving force (proportional to V_I^{FM}), at a backgate bias $V_{\mathrm{BG}} = 6.2\,\mathrm{V}$. Each lineshape is offset by $10\,\mathrm{pA}$ for clarity. **(b)** Resonance frequency shift of the first eigenmode (f_I^0) as a function of the driving force (proportional to V_I^{FM}).

5.3.6 Masses and spring constants

In order to gain insight into the vibrational properties of the device, it is useful to compare the masses and the spring constants of the nanotube and the two graphene resonators. From the built-in tension estimated above, we derive the spring constants $k_{\mathrm{G1}} = 6\,\mathrm{N/m}$ and $k_{\mathrm{G2}} = 7.4\,\mathrm{N/m}$ for graphene membranes 1 and 2, respectively. We calculate the mass and the spring constant of the nanotube by describing it as a doubly-clamped beam with no built-in tension, a good approximation for multi-wall nanotubes [91]. Using the mass density $\rho_{CNT} = 2200\,\mathrm{kg/m^3}$, the Young modulus $E = 0.3\,\mathrm{TPa}$ [91], as well as the length (1.74 μm) and diameter (17nm) of the nanotube measured with AFM, we derive a mass $m_{\mathrm{CNT}} = 0.2\,\mathrm{fg}$ and a spring constant $k_{\mathrm{CNT}} = 0.1\,\mathrm{N/m}$ for this nanotube. These values are much lower than those of the graphene resonators. This again is in line with our finding that the nanotube should only weakly couple the two graphene membranes and it should not strongly modify their mechanical modes.

5.3.7 Nonlinear mode coupling

The coupling between two duffing nonlinear mechanical resonators can lead to very interesting dynamics. Their response can be calculated by the set of equations (5.1) employing secular perturbation theory methods [60, 117] (for more information see Appendix A). When the system is driven with an oscillating frequency $\omega_{I,II}$ near its eigenfrequency $\omega_{I,II}^0$, it can be shown that the stationary solution of equations (5.1) is given by

$$|A_I|^2 = \frac{|G_I|^2}{\omega_I^{0\,2}} \frac{1}{(\epsilon^{-1}(\omega_I - \omega_I^0) - \alpha_I|A_I|^2 - \beta_I|A_{II}|^2)^2 + \Gamma_I^2}, \quad (5.2)$$

where G_I is the amplitude of the driving force that is acting on eigenmode I, $A_{I,II}$ the motion amplitude of the eigenmodes, $\alpha_{I,I}$ and $\beta_{I,II}$ are nonlinear parameters calculated

from α_1 and α_2, ϵ is a small expansion parameter that is given by $\epsilon = (Q_I Q_{II})^{-1/2}$, and Γ_I the scaled damping rate of eigenmode I.

If eigenmode I is driven in the linear regime and eigenmode II in the nonlinear, meaning that $|A_I|^2$ is small and $a_I|A_I|^2 \ll \beta_I|A_{II}|^2$, equation (5.2) predicts the frequency tuning of the first eigenmode as a square of the amplitude of the second eigenmode. In order to probe this effect we realized a pump-probe experiment as follows: The first graphene resonator, where eigenmode I is mainly localized, is probed by continuously recording its resonance lineshape with the FM technique while sweeping the frequency of the (pump) force applied to the second graphene resonator, where eignemode II is mainly localized (Figure 5.12(b)). When the applied driving forces are low and both eigenmodes remain into their linear response regime, no coupling is observed between them. When we increase the driving force on eigenmode II, the dynamics of the coupled system are changing. Figure 5.12(a) shows that the resonance frequency of eigenmode I, f_I^0, shifts when the pump frequency is swept through the resonance frequency of eigenmode II, $f_{II}^0 = 180\,\mathrm{MHz}$. This shows that the resonance frequency of one eigenmode depends on the motional amplitude of the other eigenmode, which clearly demonstrates the existence of a coupling between the two mechanical modes of the system [60, 29, 61, 118]. The asymmetric shape of the peak in f_I^0 as a function of f_{II} is attributed to the Duffing force. In another device, the shift in f_I^0 is measured as a function of the pump force amplitude that is applied on eigenmode II. This is a demonstration of the quadratic coupling which is described in equation (5.2) and can be observed not only in coupled nonlinear resonator [60], but between the modes of single nonlinear resonator [61, 118] or the modes of a laser-trapped nanoparticle [119].

We estimate that the strength of the mode coupling of the first device is about $\approx 90\,\mathrm{kHz/nm^2}$ using a shift in f_I^0 of $200\,\mathrm{kHz}$ (Figure 5.12(a)) and a motional amplitude x_{II} of $1.5\,\mathrm{nm}$. The latter is estimated in an approximate way, since we neglect the Duffing nonlinearity and use $x_{II} = QC'V_{II}^{\mathrm{AC}}V_{\mathrm{BG}}/k_{\mathrm{G2}}$ with the pump voltage $V_{II}^{\mathrm{AC}} = 40\,\mathrm{mV}$, $V_{\mathrm{BG}} = 5,8\,\mathrm{V}$, the derivative of the capacitance with respect to displacement $C' = 11\,\mathrm{pF/m}$ (estimated from the device geometry), and the measured quality factor $Q_{II} = 4000$. The eigenmode coupling of the second device is $\approx 60\,\mathrm{kHz/nm^2}$ from Figure 5.13 (x_{II} is estimated to be $\cong 1.6\,\mathrm{nm}$ for $V_{II}^{\mathrm{AC}} = 50\,\mathrm{mV}$).
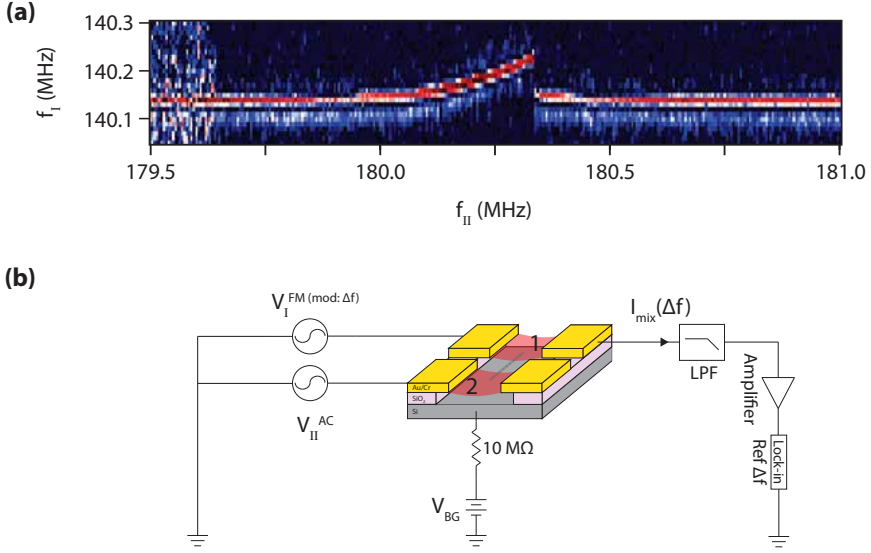
Figure 5.12: Pump-probe experiment to study the coupling between the eigenmodes. **(a)** Resonance frequency of eigenmode I as a function of the frequency of the force applied on eigenmode II. The plot is obtained by continuously measuring the mixing current of the first graphene resonator, where eginemode I is localized, as a function of the frequency f_I of the probe force, while sweeping the frequency f_{II} of the pump force. The first mode is probed with $V_{II}^{\text{FM}} = 3\,\text{mV}$, and the second mode is pumped with $V_{II}^{AC} = 40\,\text{mV}$. The gate voltage is 5.8 V. **(b)** Setup of the measurement scheme.
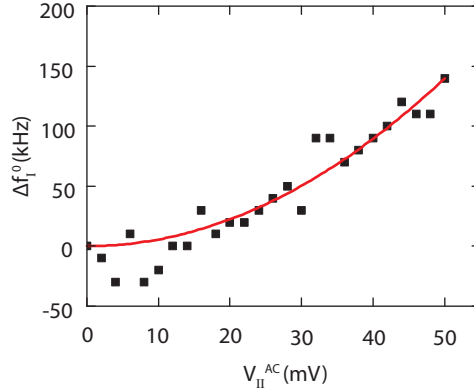

Figure 5.13: Shift of the resonance frequency of plate 1 as a function of the pump voltage applied to plate 2. The measurement corresponds to a device made from a bilayer graphene sheet, which is different from the one discussed in the rest of the Letter. The first mode is probed with $V_I^{\text{FM}} = 5\,\text{mV}$. The gate voltage is 8 V. The resonance frequencies are $f_I^0 = 189.2\,\text{MHz}$ and the $f_{II}^0 = 175.2\,\text{MHz}$. The red curve corresponds to the quadratic dependence expected from the theory of eigenmode coupling.
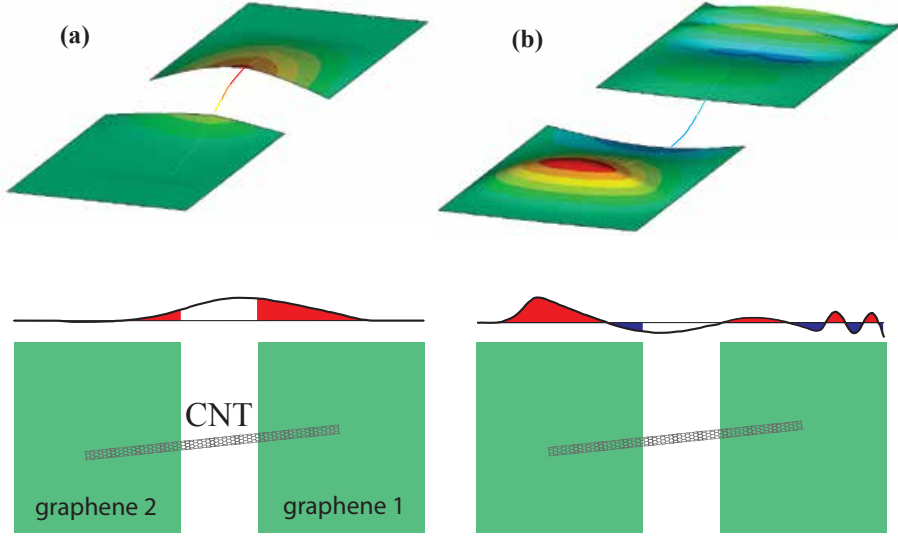
5.3.8 Finite element simulations

Figure 5.14: **(a,b)** FEM simulation image of the eigenmodes corresponding to the two measured resonances. The lower figures represent the profiles of the eigenmodes together with a (simplified) top view of the device. (Each point of the profile corresponds to the largest displacement along the width of the device.) We perform finite element simulations with ANSYS ® release 14.0 to calculate the modal shapes and modal frequencies using the geometry of the device measured by AFM. The separation between the two graphene plates is 450 nm.

The theoretical modeling that was introduced in subsection 5.3.3 and is detailed described in Appendix A, captures the behavior of the experimental structures in a great extend. To get a better insight into the dynamics of the devices, Finite Element method with ANSYS ® release 14.0 has been employed to simulate the eigenmode shapes and the corresponding resonance frequencies of the measured devices. In the FEM simulations, we assume that both ends of the nanotube are firmly attached to the graphene membrane because of the large van der Waals interaction. We also assume that the tension and the mass density remain uniform over the graphene membranes. We use the geometry of the device measured by AFM (prior to removing the silicon oxide) and the values of the built-in tension and the mass density estimated experimentally (see 5.3.4). Figure 5.14(a,b) shows two eigenmodes, one at 131 MHz and the other at 178 MHz. These values are relatively close to the measured resonance frequencies. The lower-frequency eigenmode has a sizeable amplitude in the upper graphene plate only (Figure 5.14(a)). The higher frequency eigenmode features a large displacement of the second graphene resonator (Figure 5.14(b)); the motional amplitude of the upper plate can be significant, yet it is not expected to be detected because of the shape of the mode. Indeed, this mode has several nodes, so that the motional amplitude integrated over the upper plate is low. We note that the simulations predict six more modes between the two eigenmodes. However, these additional modes are not expected to be probed in our measurements, since the associated vibrations are localized in the nanotube and/or they have a large number of nodes. In reality, the shape of the eigenmodes is very sensitive to various parameters

that are unknown, such as the spatial distributions of the contamination and of the mechanical tension. A more detailed study of the system and a quantitative estimation of the coupling will necessitate further work, such as imaging the shape of the eigenmodes [92].

5.4 Conclusions and outlook

In this chapter, we fabricated and experimentally studied the dynamics of nanomechanical systems that consist of two graphene resonators coupled by a carbon nanotube. From the technological point of view, we demonstrated the potential of modern nanofabrication techniques in realizing complex suspended vibrating structures, combining one-dimensional and two-dimensional materials. We employed electrical mixing transduction techniques to extensively characterized the complex vibrational dynamics of these devices at cryogenic temperature. Their layout allowed to independently actuate and detect the vibrations of each graphene membrane. Systematic measurements on different devices, reveal that these systems host two fundamental eigenmodes, an in-phase and an out of phase, as expected from the theory of two coupled resonators. In all studied devices, the amplitude of the each eigenmodes is localized either in the one or the other graphene resonator, while the carbon nanotube introduces only a weak linear coupling between the two individual resonators. Most interestingly though, we observed nonlinear coupling between the eigenmodes of these resonators.

Coupled resonators based on nanotube and graphene, hold promise for the study of nonlinear dynamics, such as synchronization [98, 119], chaos [60], Landau-Zener transition [120], parametric mode splitting [99], and the coherent manipulation of phonon population [99, 121]. Indeed, owing to the low dimensionality of nanotube and graphene, mechanical nonlinearities emerge at relatively low driving forces and strongly affect their dynamics [13, 29, 30, 122, 123]. Coupled mechanical resonators also offer alternate strategies to improve the quality factor [103], as well as to detect charge [108] and mass [107] with high sensitivity. In the quantum regime [7, 8, 100, 101], it has been proposed to use such nonlinear couplings between the eigenmodes for quantum nondemolition measurements [102].

Chapter 6

Brownian fluctuations in carbon nanotube resonators

In this chapter we study the Brownian fluctuations of carbon nanotube resonators, at room temperature, by coupling their motion to a focused electron beam. This work has been carried out in collaboration with Professor Pierre Verlot (Institut Lumière Matière, Université Claude Bernand Lyon 1).

In the first section we give a brief introduction. We then describe the fabrication process steps for the type of carbon nanotube mechanical resonators that were used in this study. Afterwards we describe the principle of operation of the motion transduction scheme. We then study the real-time dynamics of our devices by measuring their quadratures of motion. We study their decoherence characteristics by calculating the autocovariance of their energy and extracting their intrinsic quality factors. We compare these values with the measure mechanical linewidths and we conclude that the measured decoherence is dominated by dissipation mechanisms. We then analyze the statistics of their motion and we demonstrate that the measured nanomechanical fluctuations describe a Brownian motion of a mechanical resonator at thermal equilibrium. We then switch our attention on investigating the influence of the amorphous carbon deposition, due to the electron beam, to the mechanical properties of the nanotubes. Finally, we perform phase-coherent measurements to characterize the mass deposition in real-time.

6.1 Introduction

Nanomechanical systems [124] have recently been at the origin of a number of important advances, allowing the observation of the zero-point motion fluctuations at a macroscopic scale [7, 9, 8], the demonstration of the quantum backaction noise [10], and the creation of non-classical optomechanical states [11, 125]. The exceptional performance of nanomechanical systems primarily rely on their ultra-small effective mass m_{eff}, enabling to convert a very small force δF into a very large displacement, $\delta x_F \propto \delta F / m_{\text{eff}}$ according to Newton's Law. In this context, carbon nanotube resonators [18, 126] belong to the extreme category of nanomechanical devices: These nano-beams are the smallest mechanical transducers fabricated thus far, with effective masses reaching the attogram-range (10^{-21} kg). This remarkable property has been recently exploited to significantly improve the perfor-

mances in mass and force measurements, with carbon nanotube-based sensors reaching the yoctogram (10^{-27} kg) and the zeptonewton (10^{-21} N) detection ranges [20, 23, 17].

The performance of nanomechanical systems in sensing applications [127, 128, 129, 130, 131] are intimately related to the motion imprecision [127, 128, 132]. Upon shrinking mechanical resonators, the effects of these fluctuations can be so large that the mechanical motion becomes nonlinear [133], yielding to strongly reduced sensing abilities [122]. In particular, the presence (or not) of thermally driven nonlinear states in carbon nanotubes has recently attracted considerable attention [134, 135, 136, 137]. However, the nature of the thermal motion in carbon nanotubes remains to be addressed experimentally: Indeed, their study requires the ability to detect the mechanical fluctuations in real-time, which has been a long-standing, yet unsuccessful goal thus far. Progresses in this direction include the measurement of motion fluctuations integrated over a comparatively long time [23, 86, 79]. However, this type of measurement have been shown to be dominated by extrinsic frequency noise mechanisms [138], leaving the thermal dynamics unresolved.

In this chapter, we report the real-time measurement of nanotube resonators for the first time. We demonstrate an electron beam readout scheme enabling the detection of the instantaneous position of free-running carbon nanotube resonators. This allows us to achieve the complete characterization of their vibrational state, both in space and time domains. Despite their very large vibrational fluctuations, in the 100 nm range, our singly-clamped suspended carbon nanotube resonators behave as linear nanomechanical devices [122, 139], dominated by external dissipation mechanisms. Their trajectories describe a Brownian motion in the phase-space [140, 141], that is, both mechanical quadratures follow uncorrelated Brownian evolutions [142]. These results imply that carbon nanotube resonators are compatible with phase-coherent measurement schemes at room temperature, which we further demonstrate by implementing a piezo-driven resonant phase-locked loop which we use in order to characterize the long-term frequency dynamics in our nanomechanical systems. Our work establishes the viability of carbon nanotube resonators technology at room temperature and opens novel perspectives for the ultra-sensitive characterization, measurement and control of carbon-based nanomechanical systems.

6.2 Fabrication of singly-clamped carbon nanotube resonators

The mechanical resonators used in this work consist of singly-clamped carbon nanotubes that are anchored at the edge of highly N-doped silicon substrates (Figure 6.1). The fabrication process starts by depositing few droplets of catalyst and leaving them to dry for 1-2 minutes. Then, by blowing the sample with a controlled flow of nitrogen, most of the catalyst is remove and only few catalyst spots of various dimensions eventually stay on the sample's surface (Figure 6.1). The samples are then baked for 5 min at 150 °C, before they are inserted into the oven for the growth of carbon nanotubes, which is done by chemical vapor deposition (CVD). In this step, thermal decomposition of a CH_4 vapor is achieved in the presence of a Fe catalyst. Nanotubes are growing from the catalyst island towards all the direction. A fraction of them will be found singly-clamped suspended at the edges of the substrate (Figure 6.1). The growth temperature is at 830 °C and the growth-time is 6 min. These parameters are optimized in order to increase
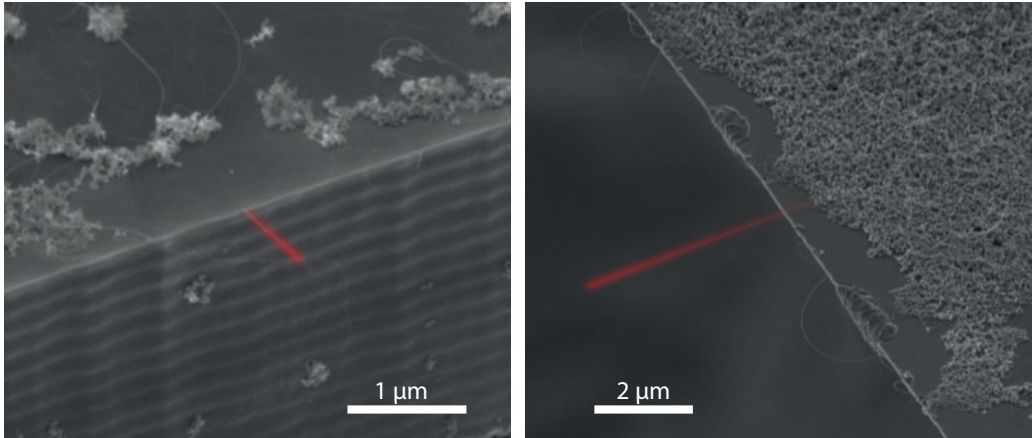
Figure 6.1: SEM images showing typical singly-clamped carbon nanotubes obtained with chemical vapour deposition (CVD) growing method. The catalyst (white particles) is spread all over the surface of a N-doped silicon substrate (darker area). After the CVD growth step, sinlgy-clamped ultra-low diameter carbon nanotubes are found at the edges of the substrate (highlighted in red, false colors).

the amount of low diameter single-walled nanotubes that are produced after the CVD growth. The length of suspended tubes is found to vary from few hundreds of nanometers to few micrometers. For the purposes of this study we specifically consider 4 distinct devices, labelled D1 to D4.

6.3   Motion detection with a focused electron beam

The detection scheme relies on coupling nanomechanical motion to a focused beam of electrons [143, 144]. Electron beams can be focused to spot sizes approaching the diameter of nanotube resonators, ensuring a much higher interaction overlap compared to usual capacitive or optical techniques used to detect nanomechanical motion [145]. The principle of the detection works as follows [144]: The collisions between the electron beam and the nanotube yield to the emission of so-called secondary electrons (SEs), which result from inelastic scattering mechanisms. The displacements of the nanotube within the electron beam create a strong modulation of the secondary electrons current, whose fluctuations are detected by means of a high bandwidth scintillator. Note that previous measurements of nanotubes using electron beams did not resolve neither the power spectrum nor the real-time evolution of their mechanical fluctuations [93, 94]. The principle of the experiment is depicted on Figure 6.2. The samples are mounted onto a 3-dimensional positioning stage hosted in a commercial Scanning Electron Microscope (SEM) (FEI Inspect F50) delivering a highly focused, ultra-low noise electron beam [144].

6.3.1   SEM scanning mode

We first operate the SEM in the conventional "scanning mode", with the electron beam being scanned over the surface of the sample and the SEs response simultaneously ac-
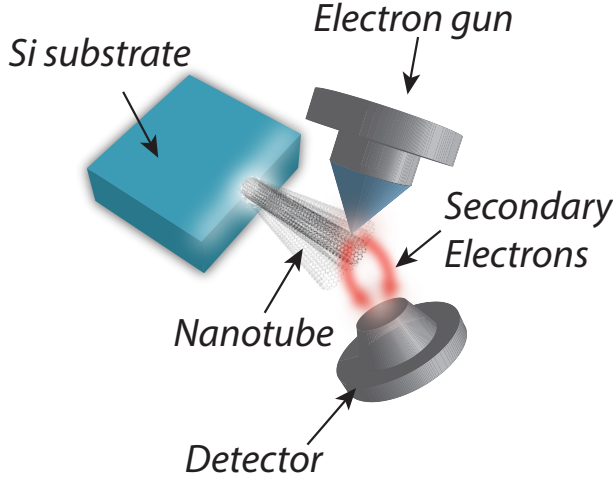
Figure 6.2: Schematic of the experimental setup. The carbon nanotube resonators are mounted inside a Scanning Electron Microscope (SEM), where their motion is detected via the Secondary Electrons (SEs) emission [143, 144], whose fluctuations are collected at the video output of the SEM and further sent to a spectrum analyser or a lock in amplifier.

quired. Figure 6.3(a) shows a typical SEs image obtained by scanning a suspended carbon nanoresonator representative of those investigated in this work (device D1). The image seems increasingly blurred towards the upper end of the nanoresonator, which is interpreted as a consequence of position noise [93, 94]. When the latter is large compared to the spatial extension of the electron beam, the integrated current $\mathcal{I}(\mathbf{r}, p) = \frac{1}{\Delta t} \int_0^{\Delta t} I(\mathbf{r}_p, t)$ becomes simply proportional to the probability $P(\mathbf{r}_p, \Delta t)$ to find the object at the electron beam position $\mathbf{r}_p$ within the integration time Δt (here I denotes the SEs emission rate). Provided that the image integration time is long with respect to the motion coherence time, the signal becomes proportional to the asymptotic probability, that is the spatial Probability Density Function (PDF) associated with the position noise [142], $P_\infty(\mathbf{r}_p) = \lim_{\Delta t \to +\infty} P(\mathbf{r}_p, \Delta t)$. For a singly-clamped, unidimensional Euler-Bernoulli beam vibrating in the scanning plane and at thermal equilibrium, this probability is given by

$$P_\infty(\mathbf{r}_\mathrm{p}) = u(\mathbf{r}_\mathrm{p} \cdot \mathbf{e}_\mathrm{CNT}) \frac{1}{\sqrt{2\pi}\sigma_\mathrm{th}} e^{-\frac{(\mathbf{e}_\mathrm{p}\mathbf{e}_1)^2}{2\sigma_\mathrm{th}^2}}, \tag{6.1}$$

with $\mathbf{e}_\mathrm{CNT}$ and $\mathbf{e}_1$ respectively denoting the axis and vibrational direction of the carbon nanotube resonator, u its fundamental mode shape [146] and σ_th^2 the thermal motion variance (the origin of the referential being taken at the anchor point of the resonator). Figure 6.3(b) shows a cross-section of Figure 6.3(a) (white, dashed arrow), confirming the Gaussian scaling of the SEs emission rate and enabling to extract a quantitative value for $\sigma_\mathrm{th} = 20.7$ nm. Images were taken for electron beam (e-beam) currents in the 0.1 nA to 100 nA range, with no significant change of the variance being observed, corroborating its thermal origin, as we will also further discuss in subsection 6.3.3.
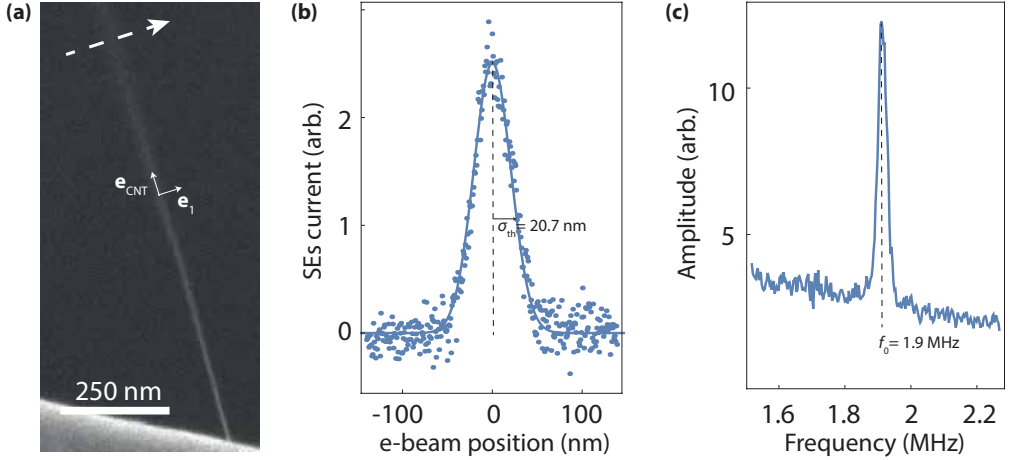
Figure 6.3: Static mechanical characterization using a SEM. **(a)** Magnified SEM micrograph showing a suspended carbon nanotube representative of those used in the present work (device D1). The image is clearly blurred towards the upper end of the nanotube, characteristic of the thermal excitation of its fundamental vibrational mode. **(b)** Intensity profile taken across the section denoted by the dashed arrow on (a). The straight line corresponds to a Gaussian fit, enabling to extract the motion variance $\sigma_{\mathrm{th}}^2 = (20.7 \text{ nm})^2$. **(c)** Power spectral density of the electromechanical signal. The SEM is operated in spot mode, the electron beam being set at the edge of the carbon nanotube. The resulting SEs fluctuations are collected at the SEM video output and further sent to a spectrum analyser. A peak is observed at the fundamental resonant frequency $\Omega_0/2\pi = 1.9$ MHz, enabling to determine the effective mass $m_{\mathrm{eff}} = K_{\mathrm{B}}T/\sigma_{\mathrm{th}}^2\Omega_0^2$.

6.3.2 SEM spot mode

To further establish the vibrational origin of this motion imprecision, we turn the SEM into "spot mode", where the electron beam is fixed at a given position. We set the electron beam at the tip of the resonator and acquire the SEs current fluctuations using a spectrum analyser (Agilent N9020A) [143, 144]. Figure 6.3(c) shows a peak centred at $\omega_0/2\pi \simeq 1.9$ MHz, consistent with the expected resonant behaviour. We verified that this peak vanishes when decoupling the electron beam from the nanoresonator, therefore identifying the peak to the fundamental mechanical resonance frequency.

The combination of the spatial PDF measurement (Figure 6.3(b)) and the spectral measurement (Figure 6.3(c)) enables to determine the static mechanical properties of the carbon nanotube resonator. The motion variance can be written as a function of the lateral spring constant k, $\sigma_{\mathrm{th}}^2 = k_B T/k$, yielding th $k \simeq 9 \times 10^{-6}$ Nm^{-1}, with the temperature $T = 300$ K. On the other hand, the spring constant expresses in terms of the spring constant and mechanical resonance frequency, $m_{\mathrm{eff}} = k/\omega_0^2 \simeq 64$ ag. From the values of the lateral spring constant and nanotube length, the radius can be evaluated on the order of $r \simeq 1.4$ nm, consistent with a nanotube containing one wall (subsection 6.3.4). We subsequently repeat this procedure for determining k and m_{eff} of all devices reported in this work.

6.3.3 Effect of the electron beam intensity in scanning mode

In this section, we consider the influence of the electron beam intensity on the motion statistic as measured in scanning mode. For simplicity, the following discussion will be performed in the one-dimensional case, without restricting generality.

The average intensity $\bar{I}(x)$ received by the carbon nanotube resonator expresses as

$$\bar{I}(x) = \int_{-\infty}^{+\infty} \mathrm{d}y \, dI^{\mathrm{in}}(y)\mathcal{P}(x-y), \tag{6.2}$$

with $I^{in}(y) = \frac{I_0}{\sqrt{2\pi}w_0}e^{-\frac{x^2}{2w_0}}$ denoting the (Gaussian) intensity profile of the electron beam (e-beam) (I_0 the e-beam intensity, w_0 the e-beam waist), $\mathcal{P}$ the position probability density function (PDF) of the carbon nanotube resonator and x the position of the electron beam, relative to the equilibrium position of the nanotube (see Figure 6.4). For an e-beam waist large compared to the nanotube diameter $w_0 \gg d$, equation (6.2) simplifies as

$$\bar{I}(x) = dI_0 Px. \tag{6.3}$$

In particular, it follows from Eq. (6.3) that the averaged secondary electron emission $\bar{I}_{\mathrm{SE}}(x) = \beta\bar{I}(x)$ (with $\hat{I}\check{s}$ the secondary electron yield) is proportional to the motion PDF of the nanotube resonator, a result which we use in order to calibrate our devices [93, 94]. Importantly, such calibration prominently relies on the assumption that the carbon nanotube resonator remains at thermal equilibrium. However, due to their extremely reduced dimensions, the dynamics of carbon nanotube resonators may be affected by the electron beam itself. In the following, we show that such effects result in strong modifications of the effectively measured motion PDF, which are not observed with our carbon nanotube resonators, ensuring that the dominant source of excitation is of a thermal origin.

Assuming that the nanomechanical motion is driven by the electron beam introduces a dependence of the PDF with respect to the average absorption rate, $I(x) \simeq dI_0\mathcal{P}(x, \tilde{I}_x)$, describing a multistable system in general. This behaviour can be understood as follows: The driving strength of the electron beam is proportional to the electron absorption rate, which increases with the probability to find the nanotube resonator within the electron beam, as shown by equation (6.3). If we assume that the nanotube resonator is initially staying at thermal equilibrium with motion variance σ_{th} (Figure 6.4(b-0)), the electron beam exposure is maximized at the center of the thermal trajectory, where the thermal motion PDF is peaking (Figure 6.4(b-1)). The effect of the electron beam is to increase the motion variance to σ_{el}, that is to spread the motion PDF, which subsequently results in a drastic decrease of the electron absorption rate (Figure 6.4(b-2)). The effect of the electron beam being reduced at this point, the nanotube resonator returns to its thermal equilibrium: Therefore, the dynamics of nanotube resonator switches back and forth between the two states (1) and (2), where it is alternately driven by the electron beam.

To give a more quantitative description of the expected dynamics in presence of electron beam driving, we further assume the e-beam driven nanomechanical state to remain Gaussian, with corresponding PDF $\mathcal{P}$ written as

$$P(x, \bar{I}(x)) = \frac{1}{\sqrt{2\pi}\sigma[\bar{I}(x)]} \exp\left\{-\frac{x^2}{2\sigma^2[\bar{I}(x)]}\right\}, \tag{6.4}$$

where $\sigma[\bar{I}(x)] = \sigma_{\text{th}}\sqrt{1 + \frac{\mathcal{P}(x)}{\mathcal{P}_{\text{th}}}\xi_{\text{e}}}$ the motion variance. Here $\mathcal{P}_{\text{th}}(x)$ demotes the thermal PDF and ξ_{e} the e-beam to thermal forces spectral densities ratio [1]. Equation (6.4) can be solved by means of pertubative approach. Witting $\mathcal{P}(x)$ as the sum of the thermal PDF plus a correction, $\mathcal{P}_{\text{th}}(x) + \tilde{\mathcal{P}}(x)$, one obtains the first order in ξ_{e}:

$$\tilde{\mathcal{P}}(x) \simeq -\sqrt{\frac{\pi}{2}}\xi_{\text{e}}\left(1 - \frac{x^2}{2\sigma_{\text{th}}^2}\right)\sigma_{\text{th}}\mathcal{P}_{\text{th}}^2(x). \tag{6.5}$$

Figure 6.4(c) shows the theoretically expected motion PDF $\mathcal{P}(x) = \mathcal{P}_{\text{th}}(x) + \tilde{\mathcal{P}}(x)$ for increasing values of ξ_{e}. Figure 6.4(c-i) shows the unchanged (thermal) PDF in absence of e-beam drive ($\xi_{\text{e}} = 0$). Figure 6.4(c-ii) shows the modified PDF for $\xi_{\text{e}} = 0.5$, that is when e-beam drive contributes to $1/3$ of the total motion fluctuations. The corresponding distribution is strongly deformed, showing important flattening and broadening. Figure 6.4(c-iii) and fig. 6.4(c-iv) show the theoretical expectation for the measured motion PDF for $\xi_{\text{e}} = 1$ and $\xi_{\text{e}} = 1.5$. An increasing splitting is observed, which is a manifestation of the above described scenario: The nanotube resonator tends to escape the central region, where e-beam driving is larger. Note that further predicting the evolution of $\tilde{\mathcal{P}}(x)$ at higher ebeam strength requires expanding equation (6.4) to higher orders, resulting in the appearance of multiple solutions around the central region, which accounts for the above mentioned multistable behaviour.

To verify the influence of the electron beam on the motion PDF, we have realized a series of images acquired at various input current. The resulting PDF where found to remain of a Gaussian nature, with no significant distortion being observed, which is a first indication that e-beam driving effects are negligible. Moreover, fitting the width of the PDF enables a quantitative determination of the motion variance, as already discussed in the main manuscript. The results are shown on fig. 6.4(d), demonstrating that the motion variance remains constant (within the measurement uncertainties) while increasing the input current over more than a decade. We therefore conclude that the effect of the electron beam remains negligible in scanning mode, the observed fluctuations being of a thermal origin.

---

[1]Note that defined as such, $S_{\text{F}^{\text{el}}} = \xi_{\text{e}}S_{\text{F}}^{\text{th}}$ (S_{F}^{th} the thermal force spectral density) corresponds to the equivalent e-beam force noise spectral density required for driving the carbon nanotube resonator into a Gaussian state with variance $\sigma_{\text{rl}} = \sqrt{\xi_{\text{e}}}\sigma_{\text{th}}$.
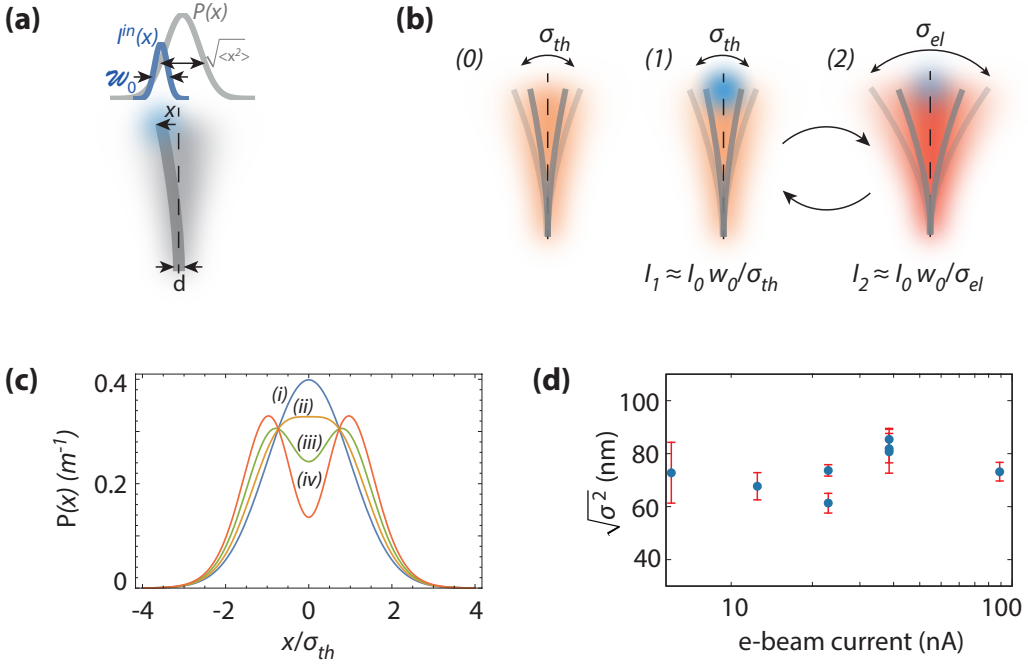
Figure 6.4: Effect of the e-beam on the motion PDF in scanning mode. **(a)** Schematic representing the geometric quantities of interest. **(b)** Schematic illustrating the expected multistable behaviour of the nanotube resonator under e-beam excitation. Initially resting at thermal equilibrium (0), the nanotube resonator is exposed to the electron beam at the centre of its Gaussian thermal trajectory, where its presence probability is maximum (1). This exposure yields to a strong mechanical excitation, resulting in a large increase of the motion variance (2). As a consequence, the presence probability is strongly reduced in the central region, resulting in a strongly reduced e-beam exposure. The nanotube resonator therefore returns to its thermal equilibrium, where it becomes again sensitive to e-beam excitation. (c) Calculated motion PDF of an e-beam driven nanotube resonator. The e-beam strength is defined relative to the thermal noise by the parameter ξ_e (see main text), with $\xi_e = 0$ (i), $\xi_e = 0.5$ (ii), $\xi_e = 1$ (iii), $\xi_e = 1.5$ (iv). (d) Motion variance as a function of the e-beam input current. Each point is obtained by fitting the corresponding second electron image using a Gaussian distribution.

6.3.4 Estimation of the diameters of carbon nanotube resonators

To estimate the diameter of our carbon nanotube resonators, we follow the protocol introduced in the work from Krishnan et al. in Ref [146]. Indeed, the motion variance σ^2 (as obtained via the Secondary Electrons (SEs) images (Figure 6.3(a))) can be further related to the physical parameters of the nanotubes via the expression [146]

$$\sigma^2 = 0.1061 \frac{L^3 k_B T}{Y r^3 G}, \qquad (6.6)$$

where L is the length of the nanotube, k_B the Boltzmann's constant, T the temperature, Y the Young's modulus, r the radius of the nanotube, and G its wall thickness. Therefore, in the case of device D1, we have measured $\sigma = 20.7$ nm and $L = 1$ μm; assuming a

Young's modulus $Y = 1.25$ TPa [146] and a single wall nanotube thickness $G = 0.34$ nm, we finally obtain a radius $r = 1.4$ nm.

6.4 Real-time dynamics

The potential of nanomechanical devices relies on their ultra-sensitive dynamical behaviour, which requires the ability to operate them close to their fundamental limits and in real-time [131, 132]. To do so, we connect the scintillator output of the SEM to an ultra-fast lock-in Amplifier (Zurich Instruments UHFLI), which we use for demodulating the quadratures of the electromechanical signal around the mechanical resonance frequency (see Appendix B). Figure 6.5(a) shows the fluctuations spectrum of the out-of-phase quadrature obtained with device D2 ($k \simeq 4.8 \times 10^{-6}$ Nm^{-1}, $m_{\text{eff}} = 938$ ag), with the demodulation frequency being set to 356 kHz. Two peaks are observed, with comparable widths and heights: Similar to what has been recently observed with larger scale singly clamped nanomechanical cantilevers [147, 148, 149], carbon nanotube resonators behave as vectorial devices, showing 2 eigendirections of vibration, which both contribute to the transduced electromechanical signal if not aligned with the SEs emission gradient [144]. Figures 6.5(b) and 6.5(c) further show the spectrum of the electromechanical signal as demodulated around each resonance frequency. The data adjust very well to Lorentzian models (straight lines), suggesting that the nanotube resonator behaves as a linearly damped, 2-dimensional harmonic oscillator at thermal equilibrium.

To address the origin of the observed mechanical linewidths [17, 138], we compute the autocovariance of the energy of the electromechanical signal $C_{I^2}(t, t+\tau) = \langle (I^2(t+\tau) - \langle I^2 \rangle)(I^2(t) - \langle I^2 \rangle)\rangle$ (see section C.1), with t the time, τ the measurement delay time, and $\langle ... \rangle$ statistical average. The energy autocorrelation has indeed the property to be insensitive towards frequency noise (see section C.3), enabling the pure extraction of the mechanical damping rates, with the additional benefit of minimal driving amplitude, therefore avoiding possible nonlinear artefacts [150]. For a linear, stationary driven non-degenerate 2-dimensional mechanical oscillator, this energy autocovariance is independent of t and can be shown to read as (see section C.2)

$$C_{I^2}(\tau) = g_1^4 \sigma_1^4 e^{-\gamma_1 \tau} + g_2^4 \sigma_2^4 e^{-\gamma_2 \tau} + 2g_1^2 g_2^2 \sigma_1^2 \sigma_2^2 e^{-\frac{\gamma_1 + \gamma_2}{2}\tau} \cos \Delta\omega\tau, \qquad (6.7)$$

with $\Delta\omega/2\pi$ the frequency splitting between the two modes and the width Γ_i, $\sigma_i^2 = \langle x_i^2 \rangle$ and $g_i = \frac{1}{\sqrt{2}} \frac{\partial I}{\partial x_i}$ the mechanical damping rate, the motion variance and the electromechanical coupling rate associated with each vibrational direction ($i \in \{1, 2\}$), respectively. The terms on the first line of equation (6.7) identify to the individual energy components associated with each mode, whereas the second line simply corresponds to the acoustic beat between the two motional polarizations. Figure 6.5(d) shows the electromechanical energy autocovariance corresponding to the spectrum shown on Figure 6.5(a). The experimental data (dots) are found to adjust very well to the theoretical model set by equation (6.7) (straight line).

It is interesting to compare the "apparent" quality factors $\tilde{Q}_i = \omega_i / \delta\omega_i$ obtained from the fits of the quadrature spectrum ($\delta\omega_i$ denoting the mechanical linewidth associated with each vibrational direction, $i \in \{1, 2\}$), to the "intrinsic" quality factors $Q_i = \omega_1 / \gamma_1$, measured via the autocovariance of the energy. The measurements presented on Figures 6.5(a) and 3(d) are consecutively repeated a number of times and used for extracting the
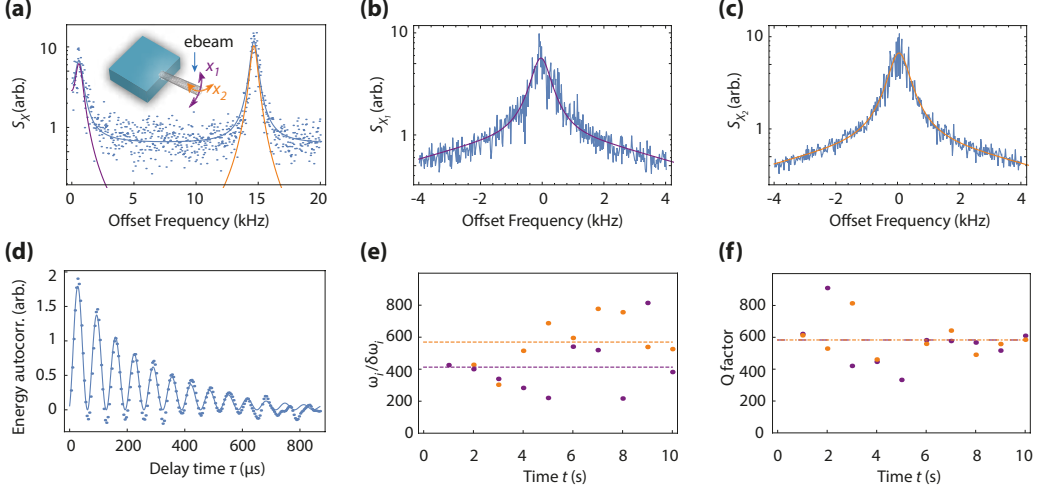
Figure 6.5: Real-time dynamics of a carbon nanotube resonator (device D2). **(a)** Motion quadrature spectrum of a free running carbon nanotube resonator. The quadratures of the electromechanical signal are demodulated at $\omega_d/2\pi = 356$kHz using an ultra-fast lock-in amplifier while the electron beam being set at the upper edge of the device. The spectrum is obtain as the Fourier transform of the 1 s-averaged autocorrelation of the out-of-phase electromechanical quadrature. Two peaks are observed, associated to the motion imprecision in each vibrational direction of the resonator. Straight lines correspond to Lorentzian adjustments (individual in purple and orange, dual incoherent sum in blue), enabling to extract both mechanical resonance frequencies $\omega_1/2\pi = 356.577$kHz and $\omega_2/2\pi = 370.243$kHz and the values of the apparent quality factors $\tilde{Q}_1 = \omega_1/\delta\omega_1 = 541$ and $\tilde{Q}_2 = \omega_2/\delta\omega_2 = 591$. **(b)** Motion spectrum associated with mode 1. The data are obtained by demodulating the electromechanical signal around frequency $\omega_1/2\pi$ and further computing the Fourier transform of its 1s-averaged autocorrelation. The straight line corresponds to a single Lorentzian fit with additional, incoherent background. **(c)** Same as (b) but for mode 2. **(d)** Electromechanical energy autocovariance calculated as $C_{I^2}(t, t + \tau) = \langle (I^2(t + \tau) - \langle I^2 \rangle)(I^2(t) - \langle I^2 \rangle) \rangle$. with I the SEs current, t the time, τ the measurement delay time, and $\langle ... \rangle$ statistical average. The straight line stands for the theoretical adjustment set by equation (6.7), yielding to the values of the intrinsic quality factors $Q_1 = 582$ and $Q_2 = 559$. **(e)** Time series of the apparent quality factors as measured from a series of spectra similar to the one shown on (a). Dashed lines correspond to the average value obtained for $\tilde{Q}_1$ and $\tilde{Q}_2$ (purple and orange, respectively). **(f)** Time series of the intrinsic quality factors as measured from a series of spectra similar to the one shown on (a). Dashed lines correspond to the average value obtained for Q_1 and Q_2 (purple and orange, respectively).

corresponding damping parameters. The results are reported on Figures 6.5(e) and 6.5(f). Dashed lines stand for the average value of each series of points, yielding to $\tilde{Q}_1 = 412$, $\tilde{Q}_2 = 570$, and $Q_1 \simeq Q_2 = 583$. These values show no significant difference between the apparent and intrinsic quality factors, which establishes that the measured decoherence is dominated by dissipation mechanisms in the carbon nanotube resonator. In other words, the Duffing restoring force and the mode-mode coupling forces, which arise from inertial nonlinear effects in singly-clamped beams [151, 152], are weak enough so that motional fluctuations do not induce sizable dephasing.

6.5 Motion statistics

We now turn our attention to the statistical analysis of nanomechanical motion. We insist that this aspect is indispensable for resolving the nature and origin of the vibrational state: Indeed, fundamental differences in vibrations, such as those reported in Refs. [8, 134, 149, 153, 154], can be resolved only by measuring their motion quadrature distribution [155]. Figure 6.6(a-i) (resp. Figure 6.6(b-i)) shows the time evolution of the motion quadratures $(X_{11}(t), X_{12}(t))$ of x_1 (resp. $(X_{21}(t), X_{22}(t))$ of x_2), defined as the cross-phase, slowly varying components of mechanical motion [141], $x_i(t) = X_{i1}(t)\cos\omega_i t + X_{i2}(t)\cos\omega_i t$. The corresponding real-time displacements $x_1(t)$ and $x_2(t)$ are shown on Figures 6.6(a-ii) and 6.6(b-ii). Figures 6.6(a-iii) and 6.6(b-iii)) show the quadratures cross-correlation functions $C_{X,i}(\tau) = \langle X_{i,1}(t)X_{i,2}(t, t+\tau)\rangle$ ($i \in \{1, 2\}$) associated with each trajectory. These correlations are found to vanish below the 10% level and can therefore be safely neglected. Figures 6.6(a-(iv,v)) and 6.6(b-(iv,v)) show the histogram of the normalized motion quadratures, which are all found to be Gaussian distributed with unit variance (straight lines). In total, these measurements show that the quadratures of the nanomechanical fluctuations in each vibrational direction describe a Brownian motion [142], consistent with a 2-dimensional mechanical resonator at thermal equilibrium. These results establish that nonlinear mechanical effects in singly-clamped nanotube resonators at room temperature remain weak. Figure 6.7(a) and Figure 6.7(b) further show the corresponding motion trajectory and associated histogram in real-space, confirming a bivariate, symmetric Normal distribution of the position noise.

To complete our study, we evaluate the spatial correlations defined as $2\sigma_1\sigma_2 C_{12}(\tau) = \langle \{X_{11}(t) + iX12(t)\}\{X_{21}(t) - iX_{22}(t)\}\rangle$ The result is reported on Figure 6.7(c), where the real and imaginary parts are shown separately. The very low level of correlations indicates that potential landscape nonlinearities have negligible effects, to first order [156, 149]. Finally, we note that the 2-dimensional, non-degenerate nature of suspended nano-cantilevers provides them with the peculiar property to develop short-term spatial correlations under random external driving, such as the one resulting from measurement backaction. These correlations manifest through strong distortions in the electromechanical spectrum [157], which are not observed in our measurements (see Figure 6.5(a) and section 6.6). This indicates the absence of any random external driving source, and in particular to the innocuity of the electron beam towards the vibrational state. Thus, the observed Brownian motion is likely to be a thermal origin.
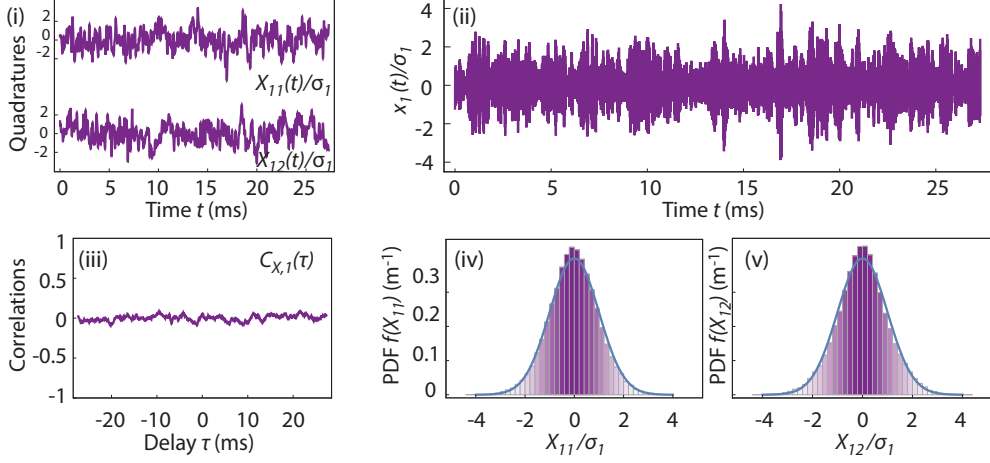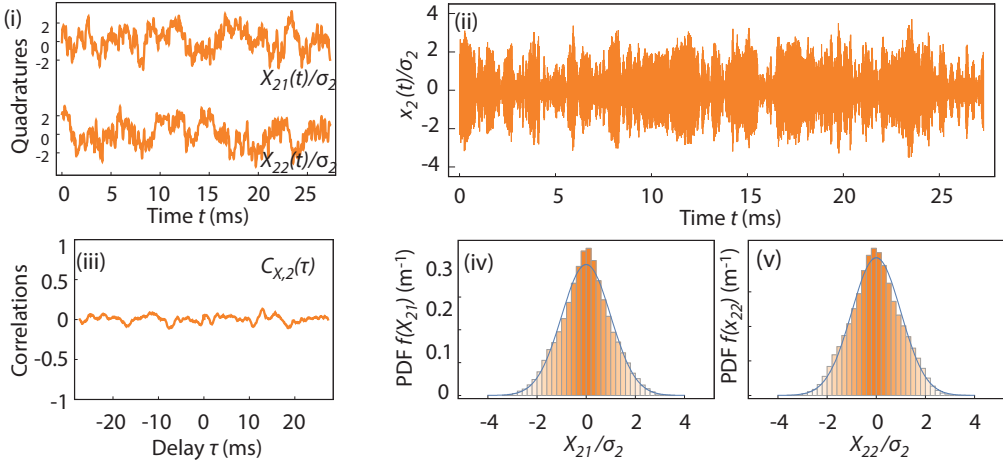
Figure 6.6: Motion statistics of a carbon nanotube resonator (device D2). **(a)** (a-i) Time evolution of the motion quadratures for mode 1. (a-ii) Corresponding real-time evolution of the position $x_1(t)$. (a-iii) Quadratures cross-correlation for mode 1. (a-iv,v) Histograms of the normalized quadratures associated with $x_1(t)$. Straight lines are Gaussian curves with unit variance. **(b)** Same as (a) for mode 2. **(c)** Nanomechanical trajectory $(x_1(t), x_2(t))$ in real-space. (d) Histogram of the nanomechanical trajectory $(x_1(t), x_2(t))$ in real- space. **(e)** Spatial correlations as a function of time. The upper and lower curves stand for the imaginary and real parts of the spatial correlation function, respectively (see text).
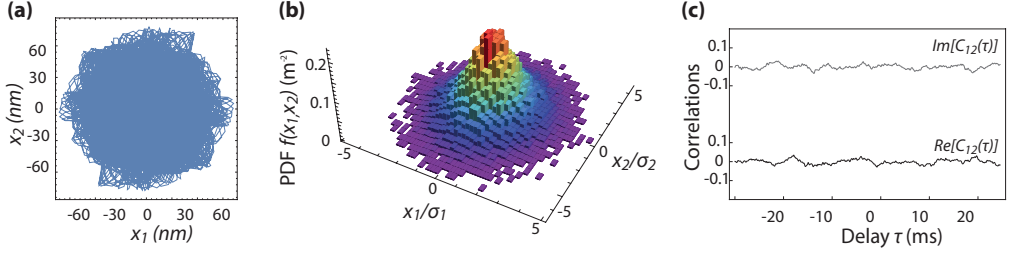
Figure 6.7: Motion statistics of a carbon nanotube resonator (device D2). **(a)** Nanomechanical trajectory $(x_1(t), x_2(t))$ in real-space. **(b)** Histogram of the nanomechanical trajectory $(x_1(t), x_2(t))$ in real-space. **(c)** Spatial correlations as a function of time. The upper and lower curves stand for the imaginary and real parts of the spatial correlation function, respectively (see text).

6.6 2-dimensional nanomechanical response

In this part we take into account the 2-dimensional motional nature of the carbon nanotube resonator, that is its ability to vibrate along two perpendicular directions $(\mathbf{e}_1, \mathbf{e}_2)$. In this basis, Newton's law can be written as:

$$m_{eff}\frac{\mathrm{d}^2 x_1}{\mathrm{d}t^2} = -k_1 x_1(t) - m_{eff}\gamma_1\frac{\mathrm{d}x_1}{\mathrm{d}t} + \mathbf{F}_{\mathrm{el}}(t) \cdot \mathbf{e}_1 + F_{\mathrm{th},1}(t)$$

$$m_{eff}\frac{\mathrm{d}^2 x_2}{\mathrm{d}t^2} = -k_2 x_2(t) - m_{eff}\gamma_2\frac{\mathrm{d}x_2}{\mathrm{d}t} + \mathbf{F}_{\mathrm{el}}(t) \cdot \mathbf{e}_2 + F_{\mathrm{th},2}(t), \qquad (6.8)$$

with $x_{1,2}(t)$ the motion trajectories along directions $\mathbf{e}_{1,2}$, $k_{1,2}$ and $\gamma_{1,2}$ the effective spring constants and linear damping rates associated with displacements $x_{1,2}$, $F_{\mathrm{th}\{1,2\}}$ the (uncorrelated) thermal forces in the eigendirections of motion, and $\mathbf{F}_{\mathrm{el}}$ the (random) force exerted by the electron beam onto the nanotube resonator. Noting $\beta = (\mathbf{e}_1, \mathbf{F}_{\mathrm{el}})$ the angle between the first motional eigendirection and the electron beam induced force, the stationary solutions of equation (6.8) write in Fourier space:

$$x_1(\omega) = \chi_1(\omega)(\cos\beta F_{\mathrm{el}}[\omega] + F_{\mathrm{th},1}(\omega))$$
$$x_2(\omega) = \chi_2(\omega)(\cos\beta F_{\mathrm{el}}(\omega) + F_{\mathrm{th},2}(\omega)), \qquad (6.9)$$

with ω the Fourier frequency, $\chi_{1,2}(\omega) = 1/2m_{eff}(\omega_{1,2}^2 - \omega^2 - i\gamma_{1,2}\omega)$ the mechanical susceptibilities associated with modes 1 and 2 ($\omega_{1,2}^2 = k_{1,2}/m_{\mathrm{eff}}$ the mechanical resonant frequencies), and $F_{\mathrm{el}} = \|\mathbf{F}_{\mathrm{el}}\|$.

Our detection scheme projects the 2-dimensional nanomechanical motion onto a given direction $\mathbf{u}_{\mathrm{m}}$ along which the linear displacement sensitivity becomes maximum [149]. The measured signal is subsequently proportional to the projected displacements x_θ given by:

$$x_\theta(t) = \cos\theta x_1(t) - \sin\theta x_2(t), \qquad (6.10)$$

where $\theta = \mathbf{e}_1 \cdot \mathbf{u}_{\mathrm{m}}$. Combining equations (6.8) and (6.9) enables to derive the output fluctuation spectrum $2\pi\delta[\omega' + \omega]S_\theta(\omega) = \langle x_\theta(\omega)x_\theta(\omega')\rangle$ (δ demoting the Dirac delta function

and $\langle ... \rangle$ statistical averaging):

$$S_\theta(\omega) = \cos^2\theta |\chi_1(\omega)|^2 S_{\mathrm{F},1}^{\mathrm{th}}(\omega) + \sin^2\theta |\chi_2(\omega)|^2 S_{\mathrm{F},2}^{\mathrm{th}}(\omega)$$
$$+ \frac{1}{2}|\chi_1(\omega)(2\cos^2\theta\cos\beta + \sin 2\theta\sin\beta) + \chi_2(\omega)(2\sin^2\theta\cos\beta - \sin 2\theta\sin\beta)|^2 S_{\mathrm{F}}^{\mathrm{el}(\omega)}.$$

(6.11)

The two first terms in equation (6.11) correspond to the (uncorrelated) thermal contributions of mode 1 and 2 as projected in the direction defined by $\mathbf{u}_{\mathrm{m}}$: In absence of any further driving term, one retrieves the usual result that linear motion detection yields to a composite spectrum whose peak amplitudes enables to determine the relative orientations of the eigenaxis of vibration [148, 149, 144]. Instead, the second line in equation (6.11) shows that the driving contribution arising from the e-beam fluctuations features the *coherent* sum of the mechanical response, where the relative phase of their response towards the e-beam noise is partially preserved: Contrary to thermal excitations, which are by nature uncorrelated along the eigen axis of vibration, the electron beam as a driving bath creates motion correlations that are characteristic of the common origin of the fluctuations when observed in two perpendicular transduction directions.

It is difficult to favor one particular mechanism that could be the dominant contribution to the electron beam backaction. In the perfect, Heisenberg limited probe case, the backaction is expected to exert along the optimal detection direction $\mathbf{u}_{\mathrm{m}}$. However quantum backaction mechanisms remain to be further investigated in the present case of electron beam assisted detection of nanotube resonators, and we prefer not to make any definitive assumption at this stage and to leave the quantum backaction force orientation (as defined by the angle β) as a free parameter. Figure 6.8 shows the evolution of the composite spectrum $S_\theta(\omega)$ for 4 different values of β covering the forward half plane ($\beta = 0°$, $45°$, $90°$, and $135°$ from Figure 6.8(a) to 6.6(d)). Each subset shows the backaction free case ($S_{\mathrm{F}}^{\mathrm{el}} = 0$, in blue) together with the full spectrum as computed from Eq. (6.11) (in yellow, with $S_{\mathrm{F}}^{\mathrm{el}} = 100 S_{\mathrm{F},\{1,2\}}^{\mathrm{th}}$), for various orientations of the eigenaxis of vibration with respect to the optimal detection direction $\mathbf{u}_{\mathrm{m}}$ ($\theta = 0°$ to $\theta = 160°$ from (i) to (ix)). The spectra have been normalized in order to better appreciate the differences induced by the presence of e-beam driving. One sees that measuring one of the eigenvibration along the optimal detection direction ($\theta = 0°$) does not enable to spectrally distinguish the thermally driven case from the e-beam driven case: In that case, the detection is simply not sensitive to the other vibrational direction and the problem is purely one-dimensional, with no difference between the thermal and the e-beam noise being spectrally possible. Instead, one observes that even for small tilts of the measurement directions relatively to the eigenaxis of vibration, the composite signal becomes immediately and strongly sensitive to the aforementioned correlations, which materialize through spectral holes being formed around frequencies that are determined by the combined mechanical and detection phases [157]: These strong spectral distortions are the signature of the presence of electron beam driving, and vice-versa. Overall, the absence of such distortions in the measured spectra indicates that the force noise induced by the electron beam is likely weaker than the thermal force noise of the nanotube.
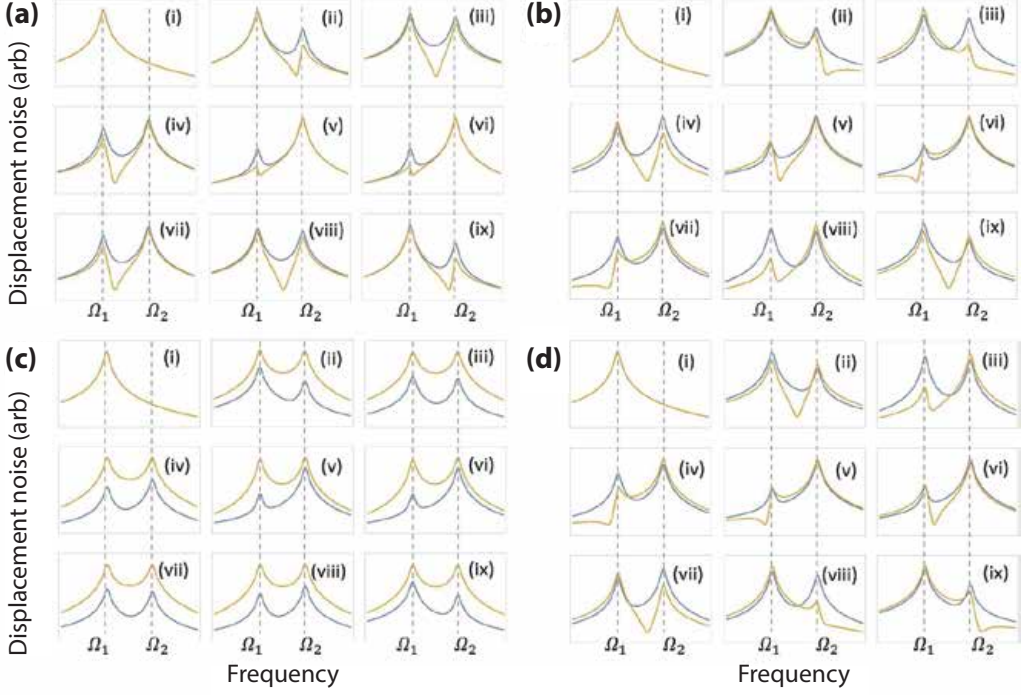
Figure 6.8: Composite detection spectrum in presence of electron beam induced driving. The composite spectrum $S_\theta(\omega)$ (eq. 6.11) is computed for 4 different force backaction orientations, $\beta = 0°$, $45°$, $90°$, and $135°$ from **(a)** to **(d)**. For each subset, both the thermal spectrum ($S_F^{el} = 0$, in blue) and the full composite spectrum (yellow) are plotted for various values of the angle θ, from $\theta = 0°$ to $\theta = 160°$ from (i) to (ix). The parameters used for evaluating equation (6.11) are $S_F^{el} = 100 S_F^{th}$, $\gamma_1 = \gamma_2$, and $\omega_2 - \omega_1 = 10\gamma_1$.

6.7 Long-term electromechanical measurements

The above presented results have been obtained on relatively short measurement time scales, in the 1 - 10 s range. On a longer timescale, electron beam exposure is known to catalyze matter deposition [158]. To quantitatively determine the impact of a prolonged e-beam exposure on the mechanical properties of the carbon nanotube resonator, we proceed as follows. We set the SEM in spot mode and expose the sample for a given time. We subsequently determine both motion variance and mechanical resonance frequency using the calibration procedure described above. The results are shown on Figure 6.9 and have been obtained with device D3 ($k = 3.7 \times 10^{-6}$ Nm^{-1}, $m_{\mathrm{eff}} \simeq 52$ ag). Figure 6.9(a) shows the scanning SEs images obtained at the beginning (left, t = 0 s) and at the end (right, t = 200 s) of the exposure. A clear deposition can be observed at the upper end of the carbon nanotube, where the electron beam spot has been set during exposure. Figure 6.9(b) and Figure 6.9(c) show the evolution of the thermal variance and mechanical resonance frequency as functions of the exposure time. The thermal variance is found to be essentially invariant in time, suggesting no change in the restoring properties of the carbon nanotube resonator. In contrast, the mechanical resonance frequency decreases as a function of exposure duration, consistent with the increase of the effective mass. Figure 6.9(d) and Figure 6.9(e) show the same results as 6.9(b) and 6.9(c) expressed in terms of the lateral spring constant and defective mass. In particular, Figure 6.9(e) enables to determine a (linear) deposition rate of 0.8 ag s^{-1}. We have verified that this deposition rate can be decreased to much lower values at lower pressure and by carefully eliminating hydrocarbon molecules from the vacuum chamber.

6.8 E-beam assisted phase-coherent measurements

An important conclusion of our work relies in the fact that our carbon nanotube resonators are found to operate in the linear regime, an indispensable prerequisite for further implementing phase-coherent measurement schemes, which are central in mechanical sensing [131]. Here we demonstrate a Phase-Locked Loop (PLL) which we use for tracking the mechanical resonance frequency in real-time. Its principle is depicted in Figure 6.10(a): a piezo actuator is driving the carbon nano-resonator close to its mechanical resonance. The phase of the resulting mechanical response is detected via the electromechanical signal and fed back to the driving oscillator, which subsequently follows the frequency changes of the nanotube resonator. The results of Figures 6.10(b) and 6.10(c) have been obtained with device D4 ($k = 1.3 \times 10^{-6}$ Nm^{-1}, $m_{\mathrm{eff}} = 260$ ag). Figure 6.10(b) shows the piezo-driven amplitude response of the nanotube resonator, with a typical doublet of resonance being observed, with respective quality factors of $\simeq 130$ and $\simeq 260$ being measured for the lower and higher frequency modes, respectively. Note that these values have been verified to match those obtained from the thermal response (see subsection 6.8.1). We set the PLL to the higher frequency mode and acquire the corresponding frequency changes, induced by e-beam hydrocarbon deposition. The mechanical frequency is found to drift with a slope $\simeq 20$ Hzs^{1}, corresponding to a deposition rate of 35 zgs^{-1}. Interestingly, the equivalent mass sensitivity, inferred from the Allan deviation of the centred frequency fluctuations, is found on the order of 16 zg for an integration time of 1 s, which is already two orders of magnitude beyond the current state of the art at room temperature [159].
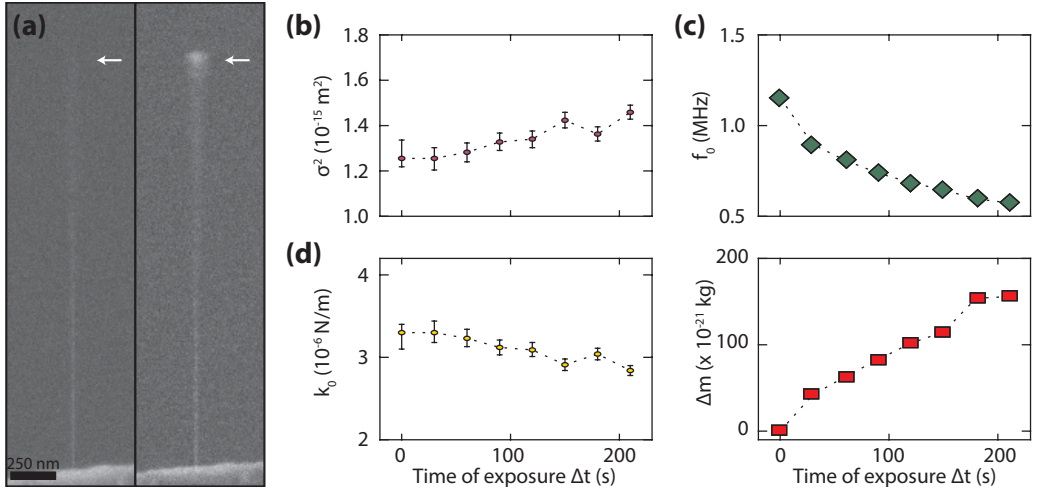
Figure 6.9: Long-term e-beam measurement (device D3). **(a)** SEs images showing the nanotube resonator at the beginning (left) and at the end (right) of the prolonged exposure sequence. **(b)** Evolution of the motion variance (as measured in scanning mode) as a function of exposure time. **(c)** Evolution of the mechanical resonance frequency (as measured in spot mode through the thermal response) as a function of exposure time. **(d)** Evolution of the lateral spring constant as deduced from (b), through the expression $k = k_B T / \sigma_{\text{th}}^2$. **(e)** Evolution of the effective mass as deduced from $m_{\text{eff}} = k_B T / \sigma_{\text{th}}^2 \omega_0^2$.
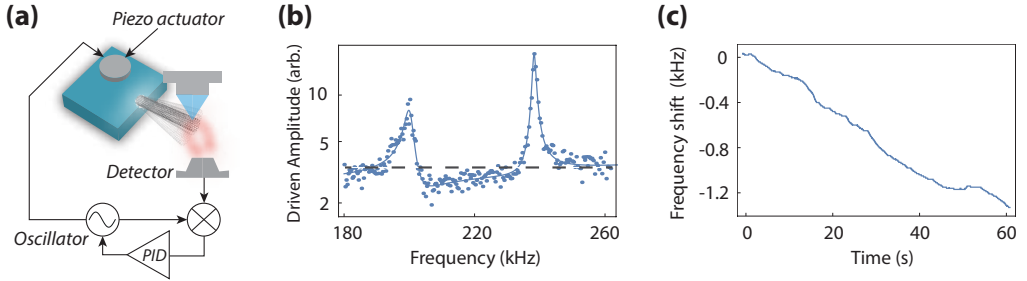

Figure 6.10: E-beam assisted phase-coherent measurements (device D4). **(a)** Simplified schematic of the piezo-driven phase-locked loop. A piezo actuator is driving the carbon nanoresonator close to its resonance. The phase of the resulting mechanical signal is detected via the electromechanical signal and fed back to the driving oscillator. **(b)** Piezo-driven frequency response of the carbon nanotube resonator. The straight, dashed line corresponds to the background associated with two independently driven harmonic oscillators. The lower displacement level in the intermediate frequency range is related to motion correlations, which result from the common excitation source for both in-plane and out-of-plane vibrational modes [157]. **(c)** Evolution of the upper resonance frequency (right peak of (b)) as a function of time. The linear frequency drift of -20 Hz s^{-1} enables to determine a mass deposition rate of 35 zg s^{-1}. The equivalent 1 s-integrated mass imprecision of 16 zg is determined as the Allan deviation of the centred frequency fluctuations, obtained after subtracting the linear drift component.
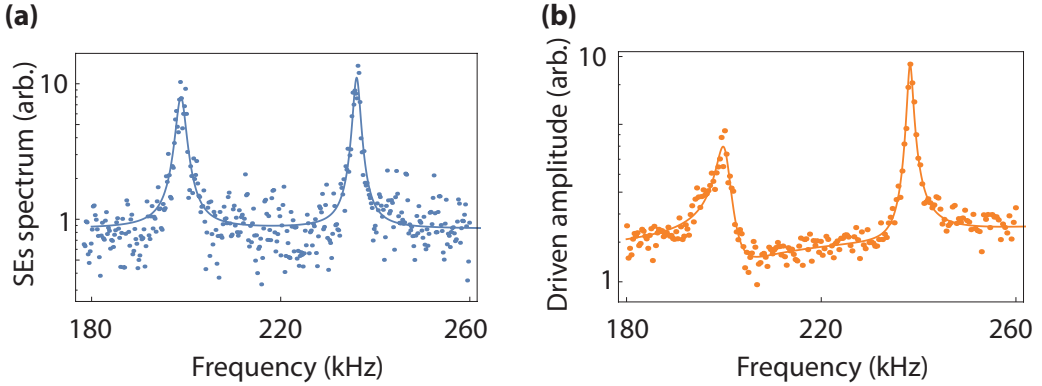
(a)

(b)

Figure 6.11: 2-dimensional incoherent and coherent response of a carbon nanotube resonator. **(a)** Thermal spectrum obtained as the fast Fourier transform of the electromechanical signal. **(b)** Piezo-driven response acquired using the ultra-fast lock-in amplifier.

6.8.1   Thermal versus driven response

In this section, we compare the piezo-driven response to the electromechanical spectrum obtained with device D4. The results are shown on Figure 6.11(a) shows the spectrum the electromechanical signal obtained as the fast Fourier Transform of the SEs current demodulated around 220 kHz. Two peaks are observed, with comparable heights and quality factors $Q_1 = 145$ and $Q_2 = 86$, respectively. These resonant peaks are in good agreement with those found from the piezo-driven response (Figure 6.11(b)) which yields to two peaks as well, with quality factors $Q_1 = 205$ and $Q_2 = 70$. We attribute the slight unbalance of the two peaks to the orientation of the piezo-induced inertial force, which is rather aligned in the direction of the second vibrational mode. Note the presence of an anti-resonance at intermediate frequencies, resulting from a negative interference between the two mode. This is perfectly captured by the theoretical adjustment, which corresponds to the coherent sum of two resonant Lorentzian curves.

6.9   Discussion

The present work demonstrates that our novel measurement method enables to detect the vibrations of nanotube-based resonators with masses as low as 50 ag. The measurement of such ultra-low mass resonators raises the question of the limits of our approach. Besides the strong, sub-nanometre confinement of the electron probe, the other key element of our scheme lies in the layout of the device. The absence of any electron scatterer within the immediate vicinity of the free-standing nano-object enables a very high SEs contrast, which is at the origin of the high motion sensitivity.

On the technical side, the sample contamination arising from e-beam exposure represents a limitation under unoptimized vacuum conditions. However it can also be viewed as a profitable tool: Indeed, as suggested above, the ability to monitor the PDF of the nanoresonator implies a nonlinear transduction mechanism, where the motion fluctuations of the probed region are large compared to the electron beam dimensions. E-beam exposure can therefore be used for linearising the electromechanical coupling, by controllably

shaping the edge of the nanotubes via electron beam assisted hydrocarbon deposition [158]. The corresponding added mass can be kept below the 10 ag range (10^{-20} kg) so that it does not significantly affect the mechanical properties of our systems. Moreover we have shown that such deposition effect can be minimized by working at lower external pressure, which can be achieved e.g. by implementing ultra-high vacuum environment.

On a more fundamental side the measurement is responsible for a random backaction that may affect the vibrational fluctuations of the measured objects [160]. While such effects are not observed in the present work (where the investigated devices are driven by thermal forces ranging between $(2 \text{ aNHz}^{-\frac{1}{2}})^2$ and $(10 \text{ aNHz}^{-\frac{1}{2}})^2$), they may become significant for nanotube resonators with higher quality factors. Indeed, e-beam quantum backaction acting on thick semiconducting scatterers has recently been evaluated to be on the order of $(1 \text{ aNHz}^{-\frac{1}{2}})^2$ under standard operating conditions [144], which should be in reach e.g. at low temperature, where the mechanical quality factors are found to be enhanced by several orders of magnitude [17]. Though certainly representing a limit from the sensing point of view, this points out that singly-clamped nanotube resonators are devices of choice for probing and controlling quantum properties of electronic beams.

Lastly, we would like to once more attract the attention on a very important and useful characteristic of our singly clamped suspended nanotube resonators, that is their 2-dimensional vibrational nature. This property makes these resonators sensitive to spatially induced motion correlations, resulting in strong distortions in their electromechanical spectrum. These signatures (such as the non-Lorentzian resonance lineshapes observed on Figure 6.10(b) in response to an external piezo drive) enable to address the presence and nature of external driving forces, with no further calibration being required [149]. In particular, it is interesting to note that these nanomechanical objects are expected to surpass the limits set by quantum backaction in principle [157], which has so far never been observed and would represent an important step from the perspective of Quantum Measurement. This 2-dimensional behaviour has also been highlighted as a strong asset in the context of ultra-sensitive nanomechanical detection, related to the corresponding ability to self-discriminate the external noise mode in phase-coherent measurements [139, 148], which will be highly beneficial to our systems.

6.10 Conclusions and outlook

We have shown that the focused electron-beam of a SEM operated in "spot mode"allows to detect the noise dynamics of attogram-scale singly-clamped suspended carbon nanotubes resonators in real-time. We have demonstrated that a SEM operated in spot mode behaves as a stereo-scope with our devices, enabling the tri-dimensional reconstruction of their motion fluctuations in real-time. We have presented a detailed analysis of the 2-dimensional noise trajectories both in space and time, and shown that such small objects behave as Brownian particles evolving in a two-dimensional harmonic potential. Our work paves the way towards the exploration of novel thermodynamic regimes at scales which have been so far inaccessible experimentally.